Cell Metabolism

Article

Bone marrow immune cells respond to fluctuating nutritional stress to constrain weight regain

Graphical abstract

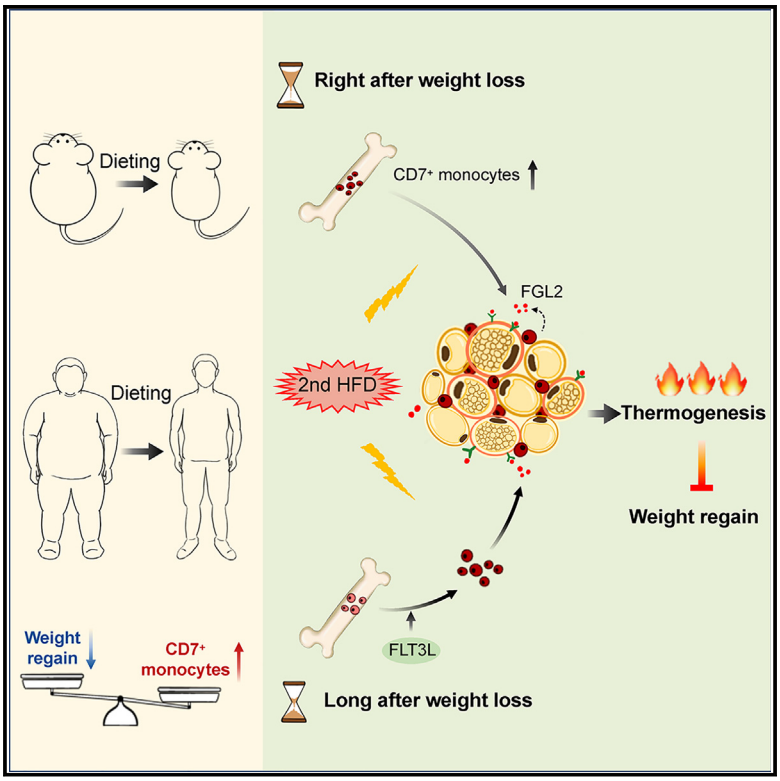

Highlights

- CD7$^+$ monocytes accumulate in the bone marrow of mice and human after weight loss
- Inducible depletion of CD7$^+$ monocytes promotes robust weight regain
- CD7$^+$ monocytes infiltrate the iWAT and promote beige fat thermogensis via FGL2
- FLT3L stimulation rejuvenates resting CD7$^+$ monocytes and constrains weight regain

Authors

Hai-Yan Zhou, Xu Feng, Li-Wen Wang, ..., Yan Huang, Qi Guo, Xiang-Hang Luo

Correspondence

xianghangluo@csu.edu.cn

In brief

Weight regain after weight loss is a major challenge in obesity treatment. Zhou et al. identify a unique CD7$^+$ monocyte population that accumulates in the bone marrow of mice and humans after weight loss. These immune cells are endowed with metabolic-memory capacities and enhance beige fat thermogenesis, thus constraining weight regain.

Zhou et al., 2023, Cell Metabolism *35*, 1915–1930
November 7, 2023 © 2023 Elsevier Inc.
https://doi.org/10.1016/j.cmet.2023.08.009

CellPress

Cell Metabolism

CellPress

Article

Bone marrow immune cells respond to fluctuating nutritional stress to constrain weight regain

Hai-Yan Zhou,[1] Xu Feng,[1] Li-Wen Wang,[1] Rui Zhou,[1] Heng Sun,[1] Xin Chen,[1] Ren-Bin Lu,[1] Yan Huang,[1] Qi Guo,[1] and Xiang-Hang Luo[1,2,3,4,5,*]

[1]Department of Endocrinology, Endocrinology Research Center, Xiangya Hospital of Central South University, Changsha, Hunan 410008, China

[2]National Clinical Research Center for Geriatric Disorders, Xiangya Hospital, Changsha, Hunan 410008, China

[3]Key Laboratory of Aging-related Bone and Joint Diseases Prevention and Treatment, Ministry of Education, Xiangya Hospital, Central South University, Changsha, Hunan 410008, China

[4]Key Laboratory of Organ Injury, Aging and Regenerative Medicine of Hunan Province, Hunan 410008, China

[5]Lead contact

*Correspondence: xianghangluo@csu.edu.cn

https://doi.org/10.1016/j.cmet.2023.08.009

SUMMARY

Weight regain after weight loss is a major challenge in the treatment of obesity. Immune cells adapt to fluctuating nutritional stress, but their roles in regulating weight regain remain unclear. Here, we identify a stem cell-like CD7$^+$ monocyte subpopulation accumulating in the bone marrow (BM) of mice and humans that experienced dieting-induced weight loss. Adoptive transfer of CD7$^+$ monocytes suppresses weight regain, whereas inducible depletion of CD7$^+$ monocytes accelerates it. These cells, accumulating metabolic memories via epigenetic adaptations, preferentially migrate to the subcutaneous white adipose tissue (WAT), where they secrete fibrinogen-like protein 2 (FGL2) to activate the protein kinase A (PKA) signaling pathway and facilitate beige fat thermogenesis. Nevertheless, CD7$^+$ monocytes gradually enter a quiescent state after weight loss, accompanied by increased susceptibility to weight regain. Notably, administration of FMS-like tyrosine kinase 3 ligand (FLT3L) remarkably rejuvenates CD7$^+$ monocytes, thus ameliorating rapid weight regain. Together, our findings identify a unique bone marrow-derived metabolic-memory immune cell population that could be targeted to combat obesity.

INTRODUCTION

Obesity is a world epidemic, leading to an increased incidence of metabolic disorders, including insulin resistance, type 2 diabetes, hypertension, and various forms of cancer.[1,2] At present, the main treatments for obesity include lifestyle and pharmacological interventions, as well as weight-loss surgery.[3–6] Unfortunately, although many of these treatments are effective initially, it is difficult to maintain more than a 10% body weight reduction.[7] Most people are prone to weight regain after appreciable weight loss.[7–10] Therefore, controlling weight regain is of prime importance in the treatment of individuals with obesity.

Obesogenic memory, the ''imprint'' left on the body after experiencing obesity, is thought to be a reason for repeated excess weight recidivism, often leading to even more severe obesity and related metabolic dysfunction.[11,12] Many studies have reported the potential mechanisms of weight regain, including changes in hormone levels, appetite stimulation, reduced energy expenditure, and metabolic adaptation.[13–15] It is reported that splenocytes, especially CD4$^+$ T cell-mediated inflammation, may contribute to obesogenic memory.[12] Further, a failure of the gut microbiome to recover properly after weight loss also represents a ''memory'' that determines the susceptibility to weight regain.[16] However, considering the complexity of whole-body homeostasis, it is interesting to speculate that there also exist anti-obesity memory cells after weight loss that could be adopted to control weight regain.

The bone marrow (BM) is a key reservoir of circulating and tissue-infiltrating immune cells. Studies have shown that obesity can cause changes in the BM microenvironment, leading to significant BM remodeling and changes in the number and function of immune cells.[17] However, how BM-localized immune cells are imprinted by obesity and reciprocally regulate weight regain is unclear.

In this study, through single-cell RNA sequencing (scRNA-seq), we identified a unique population of metabolic-memory CD7$^+$ monocytes that accumulate in the BM of mice and humans with a history of obesity and have undergone successful weight loss. These unique immune cells inhibited weight regain by preferentially migrating to the adipose tissue and inducing beiging of the white adipose tissue (WAT) through secreting fibrinogen-like protein 2 (FGL2). Of note, the BM CD7$^+$ monocytes gradually became quiescent after weight loss, while FLT3 ligand stimulation recalled these metabolic-memory features and resumed

their anti-obesity effect. Importantly, human CD7$^+$ (hCD7$^+$) monocyte proportions, which gradually decreased long after weight loss, negatively correlated with the degree of weight regain. Together, our results identify a metabolic-memory BM-derived immune cell population that offers a potential approach to counteract weight regain after appreciable weight loss.

RESULTS

Fluctuating nutritional stress endows BM immune cells with obesity-resistant properties

To test whether BM-derived immune cells might be responsible for the obesity-memory effects, we first subjected CD45.1 mice to high-fat diet (HFD) feeding for 5 weeks to induce obesity, followed by either another 3-week HFD feeding (HFD group) or switched to a 3-week normal chow diet (ND) to lose weight (cycling HFD, hereafter referred to as Cyc group).[16] Mice fed an ND throughout the 8 weeks were used as controls (ND group). At the end of 8 weeks, the body weights of mice from the Cyc group were comparable to those of mice from the ND group (Figure S1A). BM immune cells were then collected from mice of the ND, HFD, and Cyc groups and each set was then transferred into lethally irradiated wild-type (WT) CD45.2 mice (Figure 1A), and 5 weeks after reconstitution, the body weights of recipient mice were all recovered and the recipient mice were successfully reconstituted (Figures S1B and S1C). The recipient mice were then fed either an ND or an HFD to determine the effects of the adoptively transferred BM cells on body weight gain. When fed an ND, all the recipient mice showed no significant differences in body weight gain, glucose tolerance, and insulin sensitivity (Figures S1D–S1F). Surprisingly, recipient mice transferred with BM-derived immune cells collected from Cyc mice showed dramatically lower body weight regain compared with those transplanted with BM-derived immune cells either from ND or HFD mice (Figure 1B). Correspondingly, mice transferred with BM immune cells from the Cyc mice showed improved glucose tolerance, enhanced insulin sensitivity, reduced tissue weights, and smaller adipocyte sizes compared with recipient mice transplanted with BM immune cells from the HFD group (Figures 1C, 1D, S1G, and S1H). Furthermore, the brown adipose tissue (BAT) and inguinal WAT (iWAT) collected from mice transplanted with Cyc mice-derived BM immune cells showed enhanced expression of UCP1 and thermogenic genes (*Ucp1* and *Ppargc1a*) when compared with those reconstituted with BM immune cells either from the ND or the HFD group (Figures 1E and 1F), revealing a surprising role of Cyc mice-derived BM immune cells in the promotion of fat thermogenesis.

Obesity typically occurs when there is an imbalance between energy input and output.[18] To dissect the mechanism responsible for the decreased body weight gain, we measured metabolic parameters 2 weeks after recipient mice were fed an HFD, a time point when the mice began to display body weight differences. No differences in food intake and activities were observed among groups (Figures S1I and S1J). However, mice reconstituted with BM immune cells from the Cyc mice showed dramatically greater oxygen consumption and energy expenditure compared with mice transplanted with BM immune cells from the ND group or the HFD group (Figures 1G and S1K). Together, these results suggest diet switch-induced weight loss endowed BM immune cells with an unexpected capacity to enhance energy expenditure in recipient mice to main metabolic homeostasis.

scRNA-seq reveals stem cell-like CD7$^+$ monocytes accumulate in the BM of mice and humans after weight loss

To dissect the specific immune cell types accounting for the anti-obesity effects, BM immune cells were collected from mice of the ND, HFD, and Cyc groups and subjected to scRNA-seq. The proportions of myeloid cells, including monocyte-macrophages and neutrophils, were significantly elevated in the BM of HFD and Cyc mice, while the proportions of lymphoid cells, including B cells, T cells, and natural killer (NK) cells, were significantly reduced (Figure 2A). These results were in line with an obesity-related BM immune cell shift. Previous reports have suggested that CD4$^+$ T cells mediate the obesity-memory effects of weight regain.[12] Therefore, we hypothesized that myeloid cells, especially monocytes and macrophages, which present antigens and instruct the differentiation of CD4$^+$ T cells, would be responsible for the anti-obesity effects of BM immune cells from the Cyc group. The monocytes and macrophages were further divided into 6 clusters (Figures 2B and 2C), among which cluster 5 and cluster 6 showed featured increase and decrease in the Cyc mice, respectively (Figure 2C). Cell trajectory analysis revealed a gradual transition from common myeloid progenitors (CMPs) and multiple progenitor cells (MPPs), the precursors of monocytes and macrophages, to cluster 5 and terminal other clusters (Figure 2D). Kyoto Encyclopedia of Genes and Genomes (KEGG) analysis revealed that the pathways highly enriched in cluster 5 included DNA replication, ribosome biogenesis, and cell cycle (Figure S2A). Single-cell regulatory network inference and clustering (SCENIC) analysis showed that *Klf4*, *E2f1*, and *Tfdp1*, which are all related to stem cell homeostasis and cell cycle, were the top 3 transcription factors of cluster 5 (Figure 2E). Additionally, *Cd7* and FMS-like tyrosine kinase 3 (*Flt3*), both progenitor markers, were identified as top marker genes of cluster 5 (Figure 2F). Together, these results highlighted stem cell-like features of cluster 5, and we therefore defined cluster 5 as CD7$^+$ monocytes. We confirmed by flow cytometry that the frequencies of CD7$^+$ monocytes were slightly greater in the BM of HFD mice but greatly expanded in the Cyc mice compared with ND mice (Figures 2G and S2B). Consistently, CD7$^+$ monocytes were associated with an increased cell-cycle progression compared with the CD7$^-$ compartment (Figure S2C). Together, our data indicate that dieting-induced BM CD7$^+$ monocytes are characterized by stem cell-like features.

To detect the relevance of hCD7$^+$ monocytes to obesity progression, we further collected BM immune cells from age-matched male donors who were lean, obese, and those with an obesity history but succeeded in at least 10% weight loss through dieting for scRNA-seq. Similarly, the proportions of monocytes and macrophages were greater in the individuals with obesity and individuals post-dieting (Figure S2D). Within 14 clusters of monocytes and macrophages, the proportion of cluster 10 significantly expanded in the post-dieting donors and showed exclusively high expression of CD7 (Figures 2H and S2E). To test whether the hCD7$^+$ monocytes indeed correlated with metabolic status, peripheral blood cells were collected

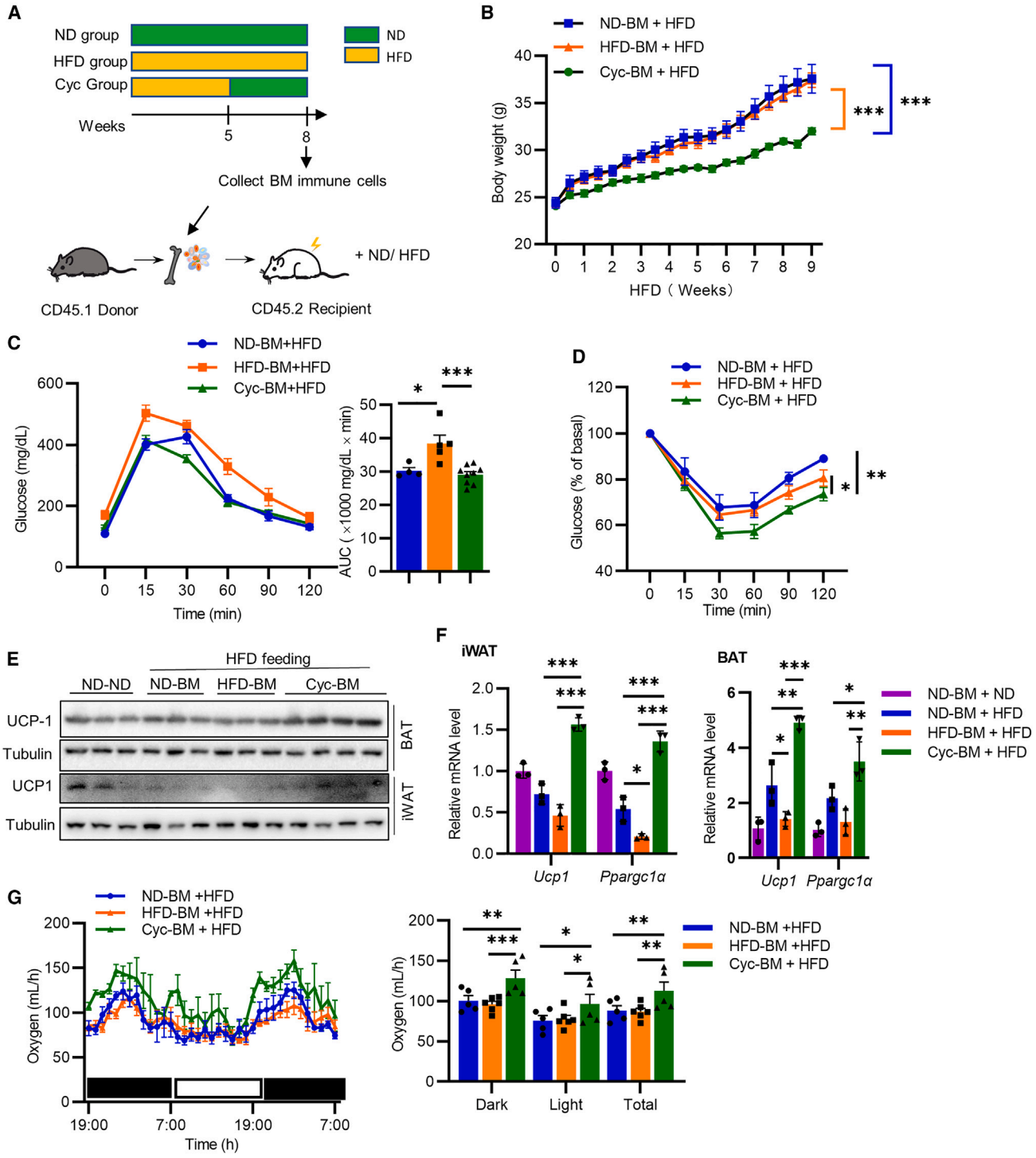

Figure 1. Fluctuating nutritional stress endows BM immune cells with obesity-resistant properties

(A) Schematic diagram for diet switch and adoptive transfer of BM immune cells.

(B–D) Analysis of metabolic performances of reconstituted recipient mice fed an HFD for 9 weeks, including (B) body weight, (C) glucose tolerance test (GTT), and (D) insulin tolerance test (ITT).

(E and F) Immunoblots of UCP1 (E) and relative mRNA levels of *Ucp1* and *Ppargc1a* (F) in the BAT and iWAT of reconstituted recipient mice fed an HFD or ND for 9 weeks.

(G) Oxygen consumption of reconstituted recipient mice 2 weeks after HFD feeding.

Data are shown as the mean ± SEM. *p < 0.05, **p < 0.01, ***p < 0.001 by one-way or two-way ANOVA or analysis of covariance (ANCOVA) test to analyze differences in oxygen consumption. (B–D) n = 4–9, (E and F) n = 3–4, and (G) n = 5–6 biological replicates.

See also Figure S1.

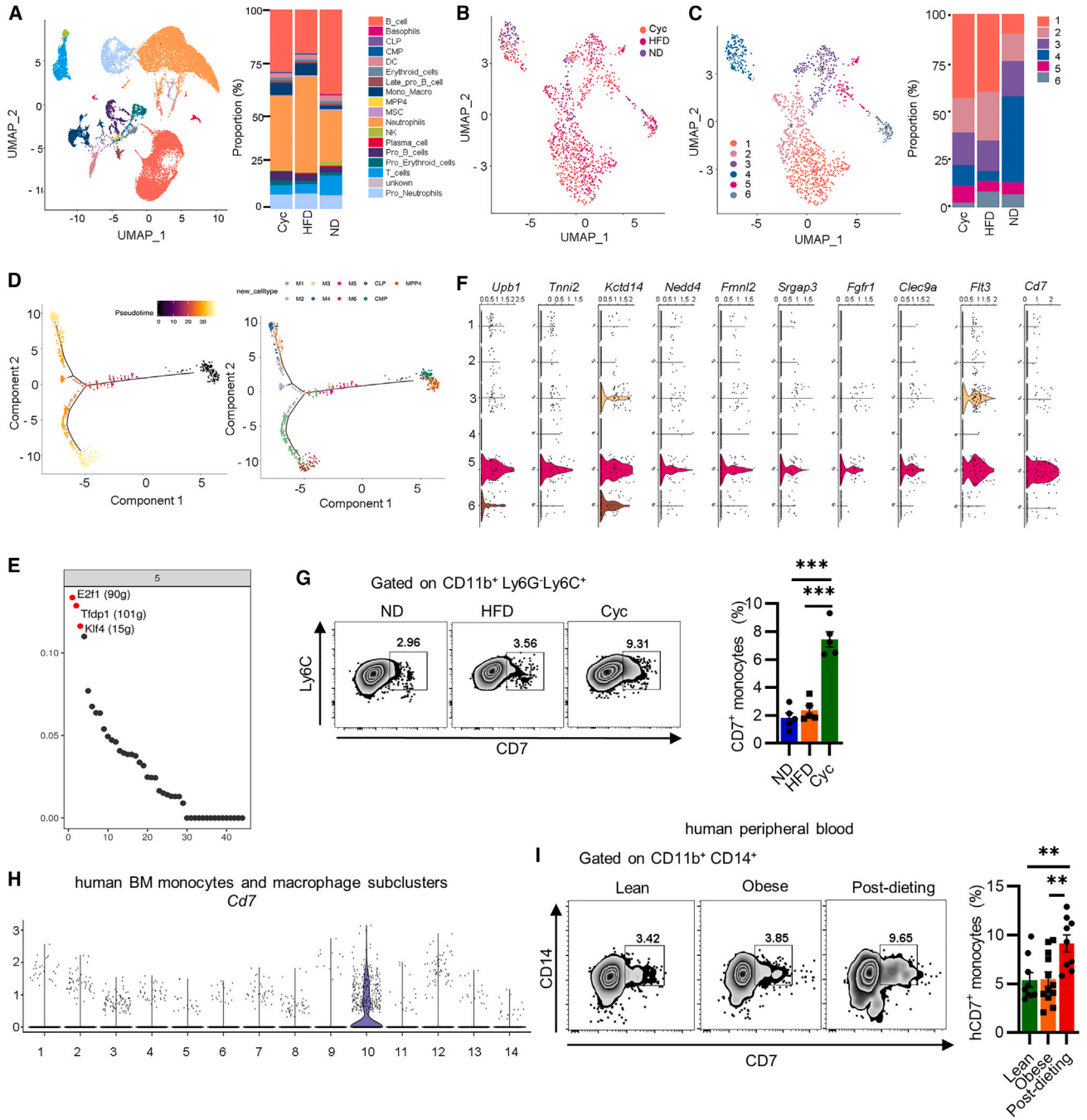

Figure 2. scRNA-seq reveals stem cell-like CD7⁺ monocytes accumulate in the BM of mice and human after weight loss

(A) Uniform manifold approximation and projection (UMAP) plot of scRNA-seq data of the BM immune cells collected from the ND, HFD, and Cyc mice.

(B and C) UMAP plots show clustering (B) of BM monocytes and macrophages based on gene expression (C) in ND, HFD, and Cyc mice.

(D) Trajectory analysis of BM monocytes and macrophage clusters.

(E) Rank for regulons in cluster 5 cells based on regulon specificity score (RSS).

(F) Violin plots show key marker gene expression of cluster 5 cells.

(G) Flow cytometry analysis of BM CD7⁺ monocytes.

(H) Violin plot of *Cd7* gene expression in monocytes and macrophage clusters of human BM.

(I) Flow cytometry analysis of human peripheral CD7⁺ monocytes from individuals who were lean, obese, or post-dieting.

Data are shown as the mean ± SEM. *p < 0.05, **p < 0.01, ***p < 0.001 by one-way ANOVA. (G) n = 5 and (I) n = 9–12 biological replicates.

See also Figure S2 and Table S1.

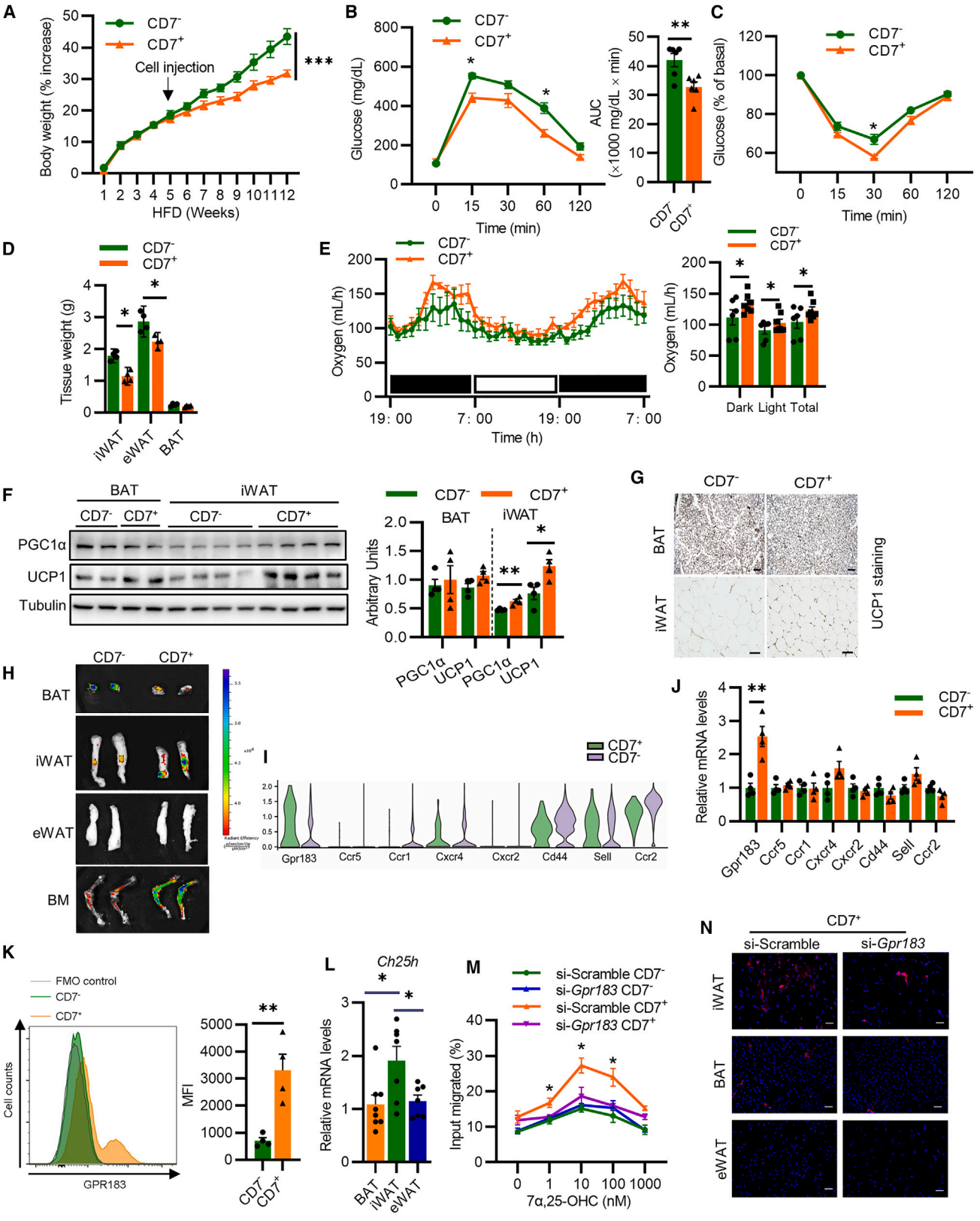

(legend on next page)

from another cohort of people based on the criteria described in the STAR Methods. Notably, in contrast to the individuals who were lean or obese, individuals post-dieting displayed a markedly high proportion of hCD7$^+$ monocytes (Figures 2I and S2F). Together, scRNA-seq reveals that CD7$^+$ monocytes, displaying stem cell-like properties, accumulate in the BM of mice and humans after weight loss, which may play a role in obesity control.

CD7$^+$ monocytes preferentially migrate to the iWAT and induce beiging

To further identify a direct role of CD7$^+$ monocytes in the regulation of obesity, BM-derived CD7$^+$ and CD7$^-$ monocytes from Cyc mice were isolated and adoptively transferred into pre-obese WT mice that were fed an HFD for 4 weeks. To be noted is that cell adoptive transfer interfered with neither the proportions nor activation status of circulating immune cells nor the circulating cytokines (Figures S3A–S3C). However, mice transferred with CD7$^+$ monocytes showed decreased body weight gain, improved glucose tolerance, alleviated insulin resistance, and reduced tissue weights (Figures 3A–3D). Notably, with approximate food intake and serum appetite hormone levels between the two groups (Figures S3D and S3E), CD7$^+$ monocytes endowed recipient mice with enhanced oxygen consumption and energy expenditure, without affecting physical activity or the respiratory exchange ratio (Figures 3E and S3F–S3H). Likewise, mice transplanted with CD7$^+$ monocytes displayed greater UCP1 and PGC1α expression in the iWAT (Figure 3F). Immunohistochemical staining showed that the UCP1 staining was greatly enhanced in the iWAT but not in the BAT (Figure 3G). Additionally, CD7$^+$ monocytes pretreatment also protected against HFD-induced obesity, indicating that CD7$^+$ monocytes can not only treat but also prevent obesity (Figure S3I).

To explore whether CD7$^+$ monocytes function via residing in the BM or through infiltrating adipose tissues, CD7$^+$ and CD7$^-$ monocytes were labeled with the lipophilic dye DiR iodide before transfer to track the trajectory of these cells *in vivo*. Consistent with the biased thermogenic promoting effect in the iWAT, CD7$^+$ monocytes, but not CD7$^-$ monocytes, preferred to localize to the iWAT, while less accumulated in the BAT and hardly accumulated in the epididymal WAT (eWAT) (Figure 3H). Through analyzing the expression of chemokine receptors, we found there was a unique upregulation of *Gpr183*, a G protein-coupled receptor mediating 7α,25-dihydroxycholesterol (7α,25-OHC) directed immune cell migration,[19–21] in CD7$^+$ monocytes, while most of the other chemokine receptors shared similar expression levels between the two cell types (Figure 3I). We further validated that the mRNA and protein levels of *Gpr183* were increased in CD7$^+$ monocytes compared with CD7$^-$ compartments (Figures 3J and 3K). Of note, the mRNA level of *Ch25h*, cholesterol 25-hydroxylase, a critical enzyme required for the generation of 7α,25-OHC,[22] was markedly higher in the iWAT than in the BAT and eWAT (Figure 3L). 7α,25-OHC concentration-dependently promoted CD7$^+$ monocytes migration; however, knockdown of *Gpr183* abolished this chemotaxis effect (Figure 3M). We further knock down *Gpr183* in isolated CD7$^+$ monocytes before they were labeled with lipophilic dye PKH26 and transferred into recipient mice. PKH26 signals in the iWAT of mice transferred with *Gpr183*-knockdown CD7$^+$ monocytes were much less than those transferred with control CD7$^+$ monocytes, indicating a GPR183-dependent preferential migration of CD7$^+$ monocytes into iWAT (Figure 3N). Consistently, mice transferred with *Gpr183*-knockdown CD7$^+$ monocytes displayed an increasing trend of body weight gain (Figure S3J).

To determine whether hCD7$^+$ monocytes could also regulate body weight and energy metabolism, hCD7$^+$ monocytes were isolated from the peripheral blood of individuals who had successfully lost weight by 10% via dieting and transferred into NOD.Cg-*Prkdc*^{scid}*Il2rg*^{em1Smoc} (NSG) mice, which lack mature T and B lymphocytes and NK cells.[23] After 4-week HFD feeding, NSG mice displayed an obvious increase in body weight and were randomized to receive either hCD7$^+$ monocytes or the hCD7$^-$ monocytes, followed by another 6-week HFD feeding (Figure S3K). Like mouse CD7$^+$ monocytes, hCD7$^+$ monocyte transfer did not affect the proportions or activation status of circulating myeloid cells (Figure S3L). The levels of circulating inflammatory cytokines and appetite hormones were also similar between the two groups (Figures S3M and S3N). Consistently, NSG mice transferred with hCD7$^+$ monocytes displayed decreased body weight gain, adipose tissue weights, improved glucose tolerance, and insulin sensitivity compared with those receiving hCD7$^-$ monocytes (Figures S3O–S3R). Together, these results demonstrate that both mouse and hCD7$^+$ monocytes possess a unique ability to combat obesity by enhancing energy expenditure.

Inducible depletion of CD7$^+$ monocytes promotes robust weight regain

To investigate the *in vivo* role of CD7$^+$ monocytes in obesity, we generated the *Cd7-Dre* mouse line that carries the Dre

Figure 3. CD7$^+$ monocytes preferentially migrate to the iWAT and induce beiging

(A–G) Percentages of body weight gain (A), GTT (B), ITT (C), tissue weights (D), oxygen consumption (E), representative immunoblots of PGC-1α and UCP1 in the BAT and iWAT (F), and representative images of UCP1 staining of the BAT and iWAT (G) (scale bars, 100 μm) of CD7$^+$ or CD7$^-$ monocytes transferred wild-type (WT) mice fed an HFD for 12 weeks.

(H) Representative *ex vivo* fluorescent images from WT mice treated with DIR-labeled CD7$^+$ or CD7$^-$ monocytes.

(I) Violin plots show gene expression of chemo-attractant receptors in CD7$^+$ monocytes based on scRNA-seq data.

(J) Relative mRNA levels of *Gpr183*, *Ccr5*, *Ccr1*, *Cxcr4*, *Cxcr2*, *Cd44*, *Sell*, and *Ccr2* in CD7$^+$ and CD7$^-$ monocytes.

(K) Flow cytometry analysis of CD7$^+$ and CD7$^-$ monocytes stained with GPR183.

(L) Relative mRNA level of *Ch25h* in BAT, iWAT, and eWAT of Cyc mice.

(M) Transwell migration of CD7$^+$ and CD7$^-$ monocytes transfected with si-Scramble or si-Gpr183 to 7α,25-OHC.

(N) Representative images of PKH26 signals tracking CD7$^+$ monocytes transfected with si-Scramble or si-*Gpr183* (red) and nucleus (blue) staining in metabolic tissues 1 week after transplantation (scale bars, 50 μm).

Data are shown as the mean ± SEM. *p < 0.05, **p < 0.01, ***p < 0.001 by one-way or two-way ANOVA or Student's t test. ANCOVA test was performed to analyze differences in oxygen consumption. (A–G) n = 4–6, (J and K) n = 4, (L) n = 7–8, and (M) n = 3 biological replicates.

See also Figure S3.

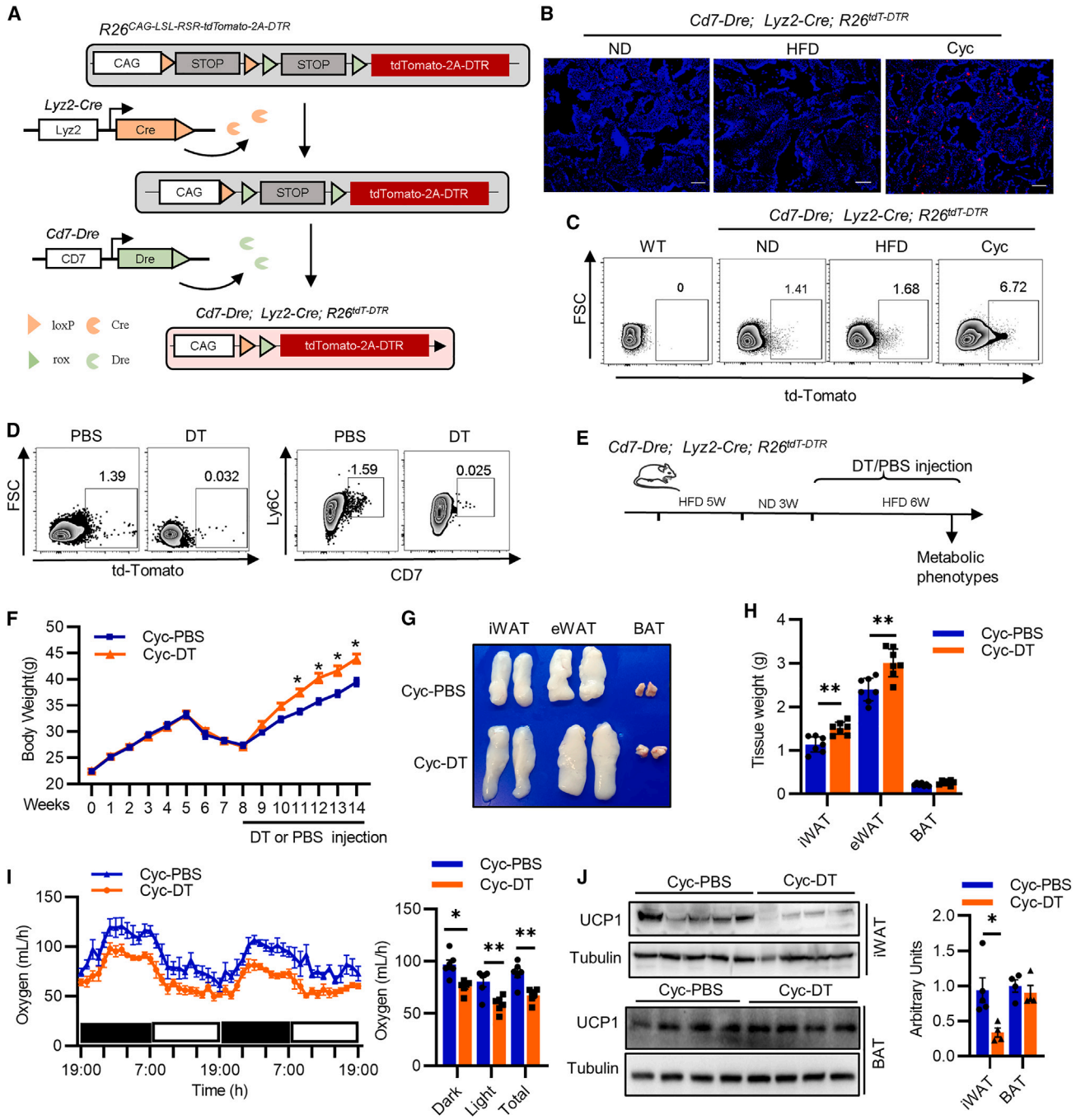

Figure 4. Inducible depletion of CD7$^+$ monocytes promotes robust weight regain

(A) Schematic diagram of breeding strategy for binary recombinase mediates synchronized lineage tracing and conditional cell subset ablation *in vivo*.

(B) Representative images of tdTomato signals in the BM of *Cd7-Dre*; *Lyz2-Cre*; *R26*$^{tdT\text{-}DTR}$ mice fed an ND, HFD, or Cyc (scale bars, 100 μm).

(C) Flow cytometry analysis of BM tdTomato$^+$ cells (gated on CD45$^+$CD11b$^+$Ly6G$^-$Ly6C$^+$) from WT mice, ND-, HFD-, and Cyc-fed *Cd7-Dre*; *Lyz2-Cre*; *R26*$^{tdT\text{-}DTR}$ mice.

(D) Flow cytometry analysis of BM tdTomato$^+$ cells and CD7$^+$ monocytes from *Cd7-Dre; Lyz2-Cre; R26*$^{tdT\text{-}DTR}$ mice treated with PBS or DT.

(E and F) Schematic diagram of diet switch and DT or PBS treatment of *Cd7-Dre; Lyz2-Cre; R26*$^{tdT\text{-}DTR}$ mice during HFD feeding (E) and corresponding body weight curve (F).

(G and H) Representative pictures (G) and tissue weights (H) of the iWAT, eWAT, and BAT from Cyc-fed *Cd7-Dre; Lyz2-Cre; R26*$^{tdT\text{-}DTR}$ mice treated with PBS or DT as in (E).

(I) Oxygen consumption of Cyc-fed *Cd7-Dre; Lyz2-Cre; R26*$^{tdT\text{-}DTR}$ mice treated with PBS or DT for 2 weeks.

(legend continued on next page)

recombinase inserted into the *Cd7* gene locus (Figure S4A) and crossed the *R26*$^{CAG\text{-}LSL\text{-}RSR\text{-}tdTomato\text{-}2A\text{-}DTR}$ mice with *Lyz2-Cre* and *Cd7-Dre* mice to achieve lineage tracing and genetic ablation of DTR-expressing CD7$^+$ monocytes after diphtheria toxin (DT) administration (Figures 4A and S4B). We confirmed by immunofluorescence and flow cytometry that BM tdTomato$^+$ cells, which showed a comparable frequency with CD7$^+$ monocytes, similarly increased in the BM post-dieting (Figures 4B and 4C). DT treatment of *Cd7-Dre;Lyz2-Cre;R26*$^{tdT\text{-}DTR}$ mice showed high efficiency in depleting both BM tdTomato$^+$ and corresponding CD7$^+$ monocytes (Figure 4D) without affecting BM immune cell composition (Figure S4C). Under ND feeding conditions, no body weight differences were observed in *Cd7-Dre;Lyz2-Cre;R26*$^{tdT\text{-}DTR}$ mice treated with DT or vehicle (Figure S4D). Then, the *Cd7-Dre;Lyz2-Cre;R26*$^{tdT\text{-}DTR}$ mice were fed a Cyc diet before consecutive treatment with DT (Cyc-DT), which allowed depletion of CD7$^+$ monocytes during weight regain (Figure 4F). Compared with PBS-treated mice, CD7$^+$ monocyte depletion evoked much more rapid and robust weight regain, accompanied with increased fat mass (Figures 4F–4H). Importantly, depletion of CD7$^+$ monocytes during HFD feeding reduced oxygen consumption and impaired cold acclimation, without affecting food intake or activity (Figures 4I and S4E–S4G). Consistently, CD7$^+$ monocyte depletion impaired UCP1 expression mainly in the iWAT, but not in the BAT (Figure 4J). Additionally, in line with the effects of CD7$^+$ monocytes in obesity control, isolated tdTomato$^+$ cells from *Cd7-Dre;Lyz2-Cre;R26*$^{tdT\text{-}DTR}$ mice also confer mice with decreased obesity (Figure S4H). Together, these results suggest that CD7$^+$ monocytes are essential for controlling weight regain.

CD7$^+$ monocytes undergo epigenetic adaptation upon nutritional stress

Immunological memory, or trained immunity, endows innate immune cells with a newfound ability to respond more rapidly and robustly to a wide variety of secondary assaults.[24,25] Here, likewise, we propose that the CD7$^+$ monocytes that expanded robustly after the diet switch represent metabolic memories that facilitate homeostasis maintenance. To probe deeper for features of CD7$^+$ monocytes during nutritional fluctuations, we performed assay for transposase-accessible chromatin with high-throughput sequencing (ATAC-seq) on isolated CD7$^+$ monocytes. The peak distribution patterns were comparable across genomic regions (Figure 5A). We detected ATAC-seq peaks that were differentially accessible between these feeding patterns (Figure 5B). Of note, the diet switch-induced peak changes largely negatively correlated with that induced by obesity (Figure 5C; Pearson R = −0.49, p < 2.2e−16). Over 14,000 peaks were induced by HFD feeding and then lost post-dieting, representing an obesity history. These lost peaks-associated genes were enriched in pathways that included oxidative stress, such as *Hif1a* and *Gapdh* (Figure 5D), which are essential for hypoxia-induced responses and anaerobic glycolysis in the BM and rapidly upregulated upon obesity. Genes with peaks that gained during obesity and lost after diet switch were also enriched in pathways of DNA damage and repair (such as *Parp1*) and inflammation (such as *Tnf*) (Figures 5D and S5A).

Additionally, around 800 peaks were established in CD7$^+$ monocytes from the HFD mice that further remained open in the Cyc mice (Figure 5E). Notably, these maintained peaks-related genes were enriched in lipid metabolism (such as *Ppara*), cell migration (such as *Peak1*), and most importantly, stem cell maintenance (such as *Klf4*) (Figures 5E and S5B), further reflecting the stem cell-like properties of CD7$^+$ monocytes. Genes with persistent open peaks also included immune suppression (such as *Tnfaip3* and *CD300a*), portraying the niche-adaptive equilibrium of CD7$^+$ monocytes in resolving inflammation (Figures 5E and S5B).

To further confirm the biased fatty acid metabolism in CD7$^+$ monocytes, we performed Seahorse Cell Mito Stress Test to determine the cellular energy metabolism. Results showed that compared with CD7$^-$ monocytes, CD7$^+$ monocytes displayed obviously enhanced oxygen consumption rates (OCRs), while the extracellular acidification rates (ECARs) were comparable (Figures S5C and S5D). Similar results were obtained when analyzing hCD7$^+$ monocytes (Figures S5E and S5F). We further carried out co-culture experiments of CD7$^+$ monocytes with CD7$^-$ monocytes or CD4$^+$ T cells, respectively, to verify whether CD7$^+$ monocytes act as anti-inflammatory "suppressive" monocytes *in vitro*. The production of inflammatory cytokines from monocytes and the cell proliferation of both CD7$^-$ monocytes and T cells in the co-culture system were not altered whenever cultured in a contact-dependent or independent manner (Figures S5G and S5H). However, the production of interferon (IFN)-γ and tumor necrosis factor alpha (TNF-α) in the co-culture system was significantly impaired when CD7$^+$ monocytes were co-cultured with T cells (Figure S5I). The suppressive function was even stronger when cells were co-cultured in a contact-dependent manner (Figure S5I). Similar results were obtained when hCD7$^+$ monocytes were co-cultured with hCD7$^-$ monocytes or hCD4$^+$ T cells (Figures S5J–S5L). Together, the reprogramming of chromatin accessibility during diet switch facilitates CD7$^+$ monocytes to maintain homeostasis.

Epigenetically regulated FGL2 mediates the effect of CD7$^+$ monocytes on beige fat thermogenesis

To further delineate the mechanism by which CD7$^+$ monocytes counteract weight regain, we cross-analyzed the peaks that displayed increasing accessibility (ATAC-seq) during fluctuating nutritional stress with featured secretory protein-encoding genes of CD7$^+$ monocytes (scRNA-seq) (Figure 6A). We identified 5 overlapping genes (*Fgl2*, *Tfrc*, *Dpp4*, *Nucb2*, and *Serpinb1a*) in these datasets, and the mRNA levels of all these 5 genes were higher in CD7$^+$ monocytes compared with the CD7$^-$ monocytes (Figure 6B). Among these genes, *Fgl2*, which

(J) Representative immunoblots of UCP1 in the iWAT and BAT of *Cd7-Dre*; *Lyz2-Cre*; *R26*$^{tdT\text{-}DTR}$ mice treated with PBS or DT for 2 weeks and subjected to cold stress for 24 h.

Data are shown as the mean ± SEM. *p < 0.05, **p < 0.01, ***p < 0.001 by two-way ANOVA or Student's t test. ANCOVA test was performed to analyze differences in oxygen consumption. (E–H) n = 7, (I) n = 6, and (J) n = 4–5 biological replicates.

See also Figure S4.

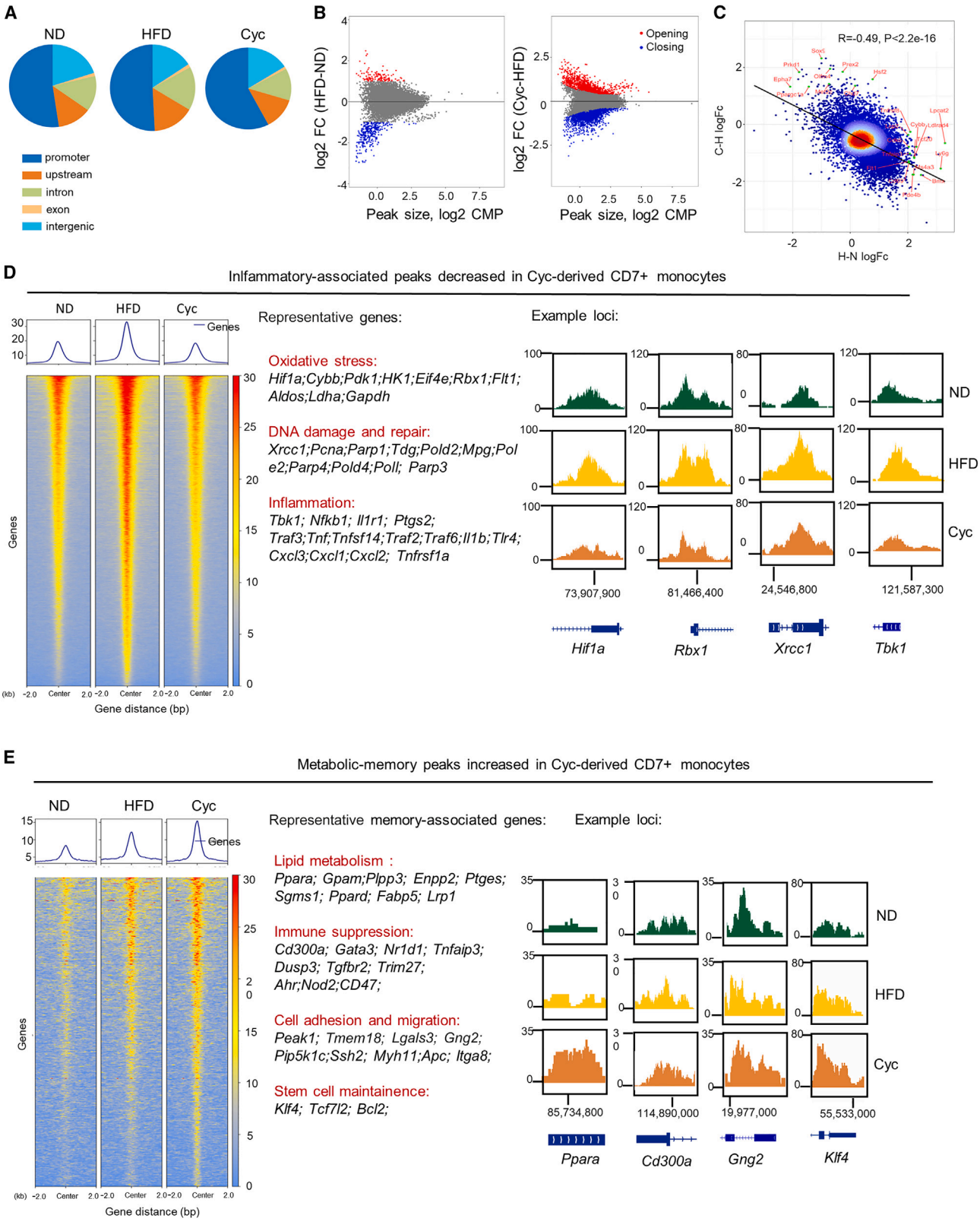

(legend on next page)

encodes for FGL2 that displays immune suppressive function,[26] showed the highest expression (Figure 6B). Genotype Tissue Expression (GTEx) database analysis showed that human *FGL2* gene expression in the whole blood positively correlates with that of *KLF4*, the marker transcription factor of $CD7^+$ monocytes (Figure S6A). Consistent with the increased chromatin accessibility of *Klf4* (Figure 5E), the peaks around the transcription start site of *Fgl2* increased in the $CD7^+$ monocytes collected from Cyc mice (Figure 6C). Also, the protein level of FGL2 was highly enriched in the culture supernatant (conditioned medium [CM]) of $CD7^+$ monocytes compared with the $CD7^-$ monocytes (Figure 6D). For these reasons, we choose *Fgl2* for further study.

Recombinant FGL2 (rFGL2)-treated mice showed dramatically enhanced the expression of thermogenic (*Ucp1*, *Ppargc1a*, *Dio2*, and *Prdm16*) and beiging-related genes (*Cd137* and *Tbx1*) in the iWAT, accompanied by enhanced cold acclimation (Figures S6B and S6C). Moreover, rFGL2-treated mice exhibited lower body weight gain, improved glucose tolerance, and enhanced insulin sensitivity when fed an HFD (Figures S6D–S6F). Further experiments showed that rFGL2 treatment activated protein kinase A (PKA) signal pathway in beige adipocytes, while treatment with the PKA inhibitor H89 abolished this effect and the downstream upregulation of UCP1 expression (Figure 6E). These results suggested that FGL2 could benefit metabolism by promoting beige fat thermogenesis. To determine the *in vivo* role of macrophage-specific FGL2, we further established macrophage-specific *Fgl2* knockout mice ($Fgl2^{\triangle Lyz2}$) by crossing *Lyz2-Cre* mice with *Fgl2*-floxed mice ($Fgl2^{f/f}$). A significant reduction of FGL2 levels was observed in the $CD7^+$ monocytes isolated from $Fgl2^{\triangle Lyz2}$ mice compared with those isolated from $Fgl2^{f/f}$ mice, indicating successful deletion of FGL2 (Figure S6G). In contrast to mice treated with rFGL2, $Fgl2^{\triangle Lyz2}$ mice were susceptible to diet-induced obesity, glucose intolerance, and insulin resistance (Figures S6H–S6J).

We next examined whether FGL2 was essential for the enhanced beige fat thermogenesis induced by $CD7^+$ monocytes. Beige adipocytes were treated with CM of $CD7^+$ and $CD7^-$ monocytes, and results showed that the CM of $CD7^+$ monocytes promoted UCP1 and PGC1α expression in beige adipocytes compared with that from $CD7^-$ monocytes (Figure 6F). However, the CM of $CD7^+$ monocytes isolated from $Fgl2^{\triangle Lyz2}$ mice significantly subdued fat thermogenesis compared with that of $CD7^+$ monocytes isolated from control littermates, while supplementation of rFGL2 restored expression of UCP1 and PGC1α (Figure 6F). We further investigated the involvement of FGL2 in $CD7^+$ monocytes-mediated anti-obesity effects *in vivo*. $CD7^+$ and $CD7^-$ monocytes were isolated from $Fgl2^{f/f}$ and $Fgl2^{\triangle Lyz2}$ mice that fed a Cyc regime and transferred into pre-obese WT mice followed by HFD feeding. Notably, *Fgl2* deficiency greatly impaired the anti-obesity effects of $CD7^+$ monocytes (Figure 6G).

We next conducted mass spectrometry analysis to screen the potential receptors of FGL2 in beige adipocytes. We selected the reported canonical receptors with the top 5 scores in the results for further evaluation (Figure 6H). qPCR analysis revealed that the expression of TMEM120A, which has been reported to regulate lipid metabolism,[27] was higher than other receptors in beige adipocytes (Figures 6I and 6J). Immunoblot analysis further demonstrated that TMEM120A was highly expressed in adipocytes other than other cell types in the adipose tissue, while its expression in the BM was quite low (Figure 6K). Thus, we chose TMEM120A for further study.

To test whether FGL2 can bind to TMEM120A in beige adipocytes, we first performed molecular docking of mouse TMEM120A and FGL2. Multiple groups of residues could form hydrogen bonds between FGL2 and TMEM120A (Figure S6K), indicating a robust binding possibility. We further transfected FLAG-FGL2 and HA-TMEM120A plasmids into the human embryonic kidney (HEK) 293T cells and then collected the cell lysate for co-immunoprecipitation (coIP) assay. Results validated that FGL2 could bind to TMEM120A (Figure 6L). To further identify the domain of FGL2 responsible for the interaction, we generated a series of FLAG-tagged FGL2 deletion mutants based on different domain positions. Although deletion mutants that lost nucleotides 1–70 still bound TMEM120A, depletion of nucleotides between 71–157, 100–122, and 197–429 in FGL2 abolished their binding with TMEM120A, indicating that these domains are responsible for the interaction of FGL2 with TMEM120A (Figure S6L).

To prove that TMEM120A mediates the effects of FGL2 on beige adipocyte thermogenesis, we transfected beige adipocyte with TMEM120A small interfering RNA (siRNA) or scramble control siRNA. The activation of cyclic AMP (cAMP)-PKA signaling and downstream thermogenic gene expression (*Ucp1* and *Ppargc1a*), which was stimulated by rFGL2 treatment, was all inhibited by the absence of TMEM120A (Figures 6M and S6M). Thus, we concluded that FGL2 binds to TMEM120A and promotes beige adipocyte thermogenesis.

FLT3 ligand stimulation rejuvenates $CD7^+$ monocytes and thus inhibits weight regain

A growing body of evidence has shown that established trained immunity disappears gradually long after resolution.[28,29] We next explored whether BM immune cells from Cyc mice could protect against obesity long after weight loss. Mice were fed an HFD for 5 weeks and then switched to ND feeding for either 3 weeks (Cyc), 6 weeks (Cyc-6w), or 10 weeks (Cyc-10w), respectively. Compared with those transferred with BM immune cells from Cyc mice, mice transferred with BM immune cells from Cyc-6w and Cyc-10w mice showed little effect on obesity progression and oxygen consumption (Figures 7A and S7A).In line with this, the BM immune cells collected from either the Cyc-6w or

Figure 5. $CD7^+$ monocytes undergo epigenetic adaptation upon nutritional stress

(A) Genomic distribution of ATAC-peaks in $CD7^+$ monocytes.

(B) Log_2 fold change (HFD-ND) (left) and log_2 fold change (Cyc-HFD) (right) versus read counts per million (log_2CPM) from ATAC-seq differential analyses. Differentially opening/closing peaks are represented in red/blue.

(C) Correlation of ATAC-seq remodeling between Cyc versus HFD and HFD versus ND. Blue-red gradient on data points represents their relative local density.

(D and E) Density plots depicting ATAC-seq signals at summits ±2 kb of inflammatory-associated peaks (D) and metabolic-memory peaks (E) in $CD7^+$ monocytes with heatmap of individual peaks beneath. Representative genes are shown (middle). The right panel is snapshots of genomic loci.

See also Figure S5.

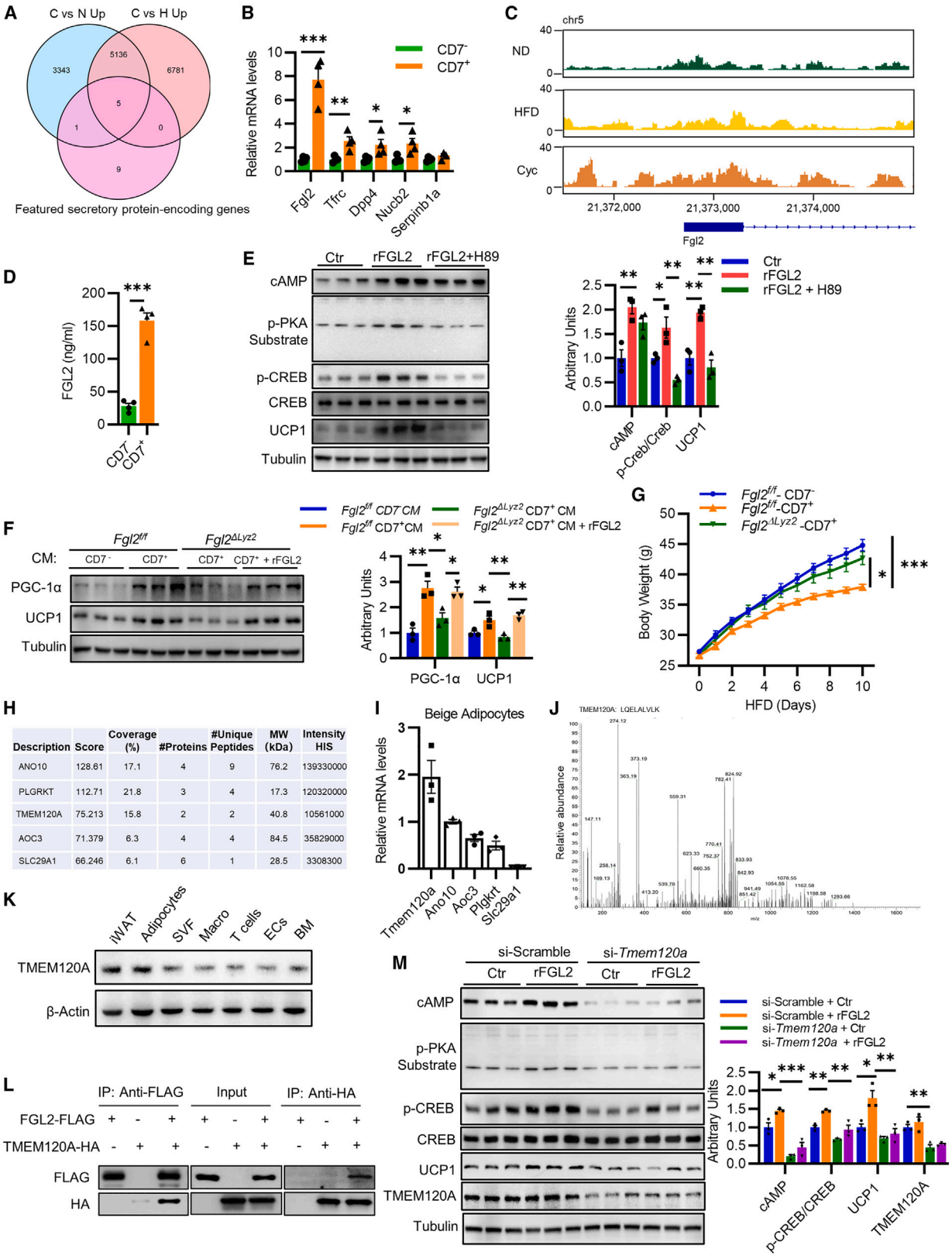

(legend on next page)

Cyc-10w mice showed decreased frequencies of CD7$^+$ monocytes (Figure 7B). Besides, the cell-cycle progression of CD7$^+$ monocytes isolated from Cyc-6w and Cyc-10w mice was greatly suppressed compared with those isolated from Cyc mice (Figure 7C), indicating CD7$^+$ monocytes gradually entered a quiescent state after weight loss.

To detect the clinical relevance, we recruited a cohort of volunteers with obesity (age and sex matched) who were instructed to undergo successful weight loss (at least 10%) through dieting. The frequencies of hCD7$^+$ monocytes in the peripheral blood gradually decreased over time after weight loss (Figure 7D). Those who succeeded in maintaining more than 10% weight loss for at least 6 months possessed even higher proportions of hCD7$^+$ monocytes compared with those who failed to do so (Figure 7D). Consistently, the subcutaneous adipose tissue of participants maintaining weight loss showed more hCD7$^+$ monocyte infiltration than that of participants with relevant weight regain (Figure 7E). Moreover, the frequencies of circulating CD7$^+$ monocytes were negatively associated with the degree of weight regain 6 months after weight loss (Figure 7F). Together, these results suggest that evoking CD7$^+$ monocytes in those long after weight loss may help to combat weight regain.

As *Flt3* gene tops the CD7$^+$ monocytes and FLT3 is a BM factor playing an important role in hematopoietic development,[30] we thus conjectured that stimulation with FLT3 ligand (FLT3L) may rejuvenate CD7$^+$ monocytes and therefore restore metabolic homeostasis. To test this hypothesis, we first examined the levels of *Flt3l* in the BM and found that its expression gradually decreased after weight loss (Figure 7G), concurrent with the decreased CD7$^+$ monocytes and failure to control obesity. Remarkably, FLT3L stimulation greatly induced the frequencies of CD7$^+$ monocytes *in vitro* (Figure S7B). Moreover, FLT3L stimulation promoted *Fgl2* mRNA and protein levels in CD7$^+$ monocytes in a dose-dependent manner (Figures S7C and S7D). We further found that Cyc-10w mice, which were stimulated with FLT3L for 2 weeks, showed boosted CD7$^+$ monocytes both in the BM and circulation (Figure 7H). To systemically dissect the reprogramming landscape of CD7$^+$ monocytes stimulated by FLT3L, the CD7$^+$ monocytes of Cyc, Cyc-10w, and FLT3L-stimulated Cyc-10w mice were subjected to ATAC-seq (Figure S7E). The peak distribution patterns were comparable across genomic regions, while FLT3L stimulation induced peak changes that negatively correlated with those induced in resting Cyc-10w mice (Pearson R = −0.38, p < 2.2e−16) (Figures S7F and S7G). We found that 5,880 peaks were lost during resting and resumed by FLT3L stimulation (Figure 7I). Genes associated with the rescued peak were enriched in the FoxO and phosphatidylinositol 3-kinase (PI3K) pathways (Figure S7H), both of which are critical pathways for coordinating memory immune cell differentiation.[31] Genes with resumed peaks were also involved in oxidative phosphorylation (such as *Ndufa8* and *Cox5b*) and stem cell homeostasis (such as *Klf4* and *Tfdp1*) (Figure 7I). Moreover, rejuvenated migration and immune suppressive function were also observed (related genes included *Gpr183*, *Icosl*, and *Il10*) (Figure 7I). Of note, peaks around the transcription start site of *Klf4* and *Fgl2* were also restimulated by FLT3L (Figure S7I), further demonstrating a critical role of FLT3L stimulation in rejuvenating CD7$^+$ monocytes.

To determine whether the boosted CD7$^+$ monocytes recuperated the capacity against weight regain, Cyc-10w mice were injected with FLT3L or vehicle three times a week for 10 weeks. Importantly, FLT3L treatment succeeded in restraining weight regain of Cyc-10w mice when subjected to a secondary HFD feeding (Figure 7J). FLT3L was reported to enhance other cell types, including dendric cells (DCs) and common lymphoid progenitors (CLPs),[32] and we noticed that FLT3L stimulation still had certain obesity-suppressive effects in *Fgl2*$^{\triangle Lyz2}$ mice (Figure S7J). To further highlight the significance of CD7$^+$ monocytes in mediating the obesity control function of FLT3L, Cyc-10w *Cd7-Dre; Lyz2-Cre;R26*$^{tdT\text{-}DTR}$ mice were injected with DT every 3 days to persistently deplete CD7$^+$ monocytes during secondary HFD feeding. Notably, without CD7$^+$ monocytes, FLT3L stimulation no longer displayed a restraining effect on weight regain (Figure 7K). These results suggest that FLT3L stimulation rejuvenates CD7$^+$ monocytes and consequently inhibits weight regain.

DISCUSSION

Considerable efforts have been devoted to the development of effective weight reduction strategies, yet many dieting individuals fail to maintain long-term weight reduction, and instead undergo cycles of excessive weight regain. Thus far, efforts to

Figure 6. Epigenetically regulated FGL2 mediates the effect of CD7$^+$ monocytes on beige fat thermogenesis

(A) Venn diagram shows CD7$^+$ monocytes featured secretory protein-encoding genes that gained increased chromatin accessibility during diet switch.
(B) Relative mRNA levels of *Fgl2*, *Tfrc*, *Dpp4*, *Nucb2*, and *Serpinb1a* in CD7$^+$ and CD7$^-$ monocytes from Cyc mice.
(C) Genomic loci snapshots of *Fgl2* chromatin peaks that gained accessibility in Cyc mice.
(D) FGL2 protein levels in culture medium of CD7$^+$ and CD7$^-$ monocytes from Cyc mice.
(E) Representative immunoblots of cAMP, p-PKA substrate, phosphor-CREB, CREB, and UCP1 in beige adipocytes treated with vehicle, recombinant FGL2 (rFGL2) with or without PKA inhibitor H89.
(F) Representative immunoblots of PGC-1α and UCP1 in beige adipocytes treated as indicated.
(G) The body weight curve of WT mice transferred with CD7$^+$ or CD7$^-$ monocytes from *Fgl2*$^{f/f}$ or *Fgl2*$^{\triangle Lyz2}$ mice as indicated.
(H) List of candidate membrane receptors of FGL2 with top 5 scores in mass spectrum analysis.
(I) Relative mRNA levels of *Ano10*, *Tmem120a*, *Aoc3*, *Plgkrt*, and *Slc29a1* in beige adipocytes.
(J) Mass spectrogram of identified TMEM120A protein binding to FGL2.
(K) Representative immunoblots of TMEM120A in different cells as indicated.
(L) Co-immunoprecipitation analysis of FLAG-FGL2 (left) and HA-TMEM120A (right) binding.
(M) Representative immunoblots of cAMP, p-PKA substrate, phosphor-CREB, CREB, UCP1, and TMEM120A in beige adipocytes transfected with si-Scramble or si-*Tmem120a* in the presence of vehicle or FGL2.
Data are shown as the mean ± SEM. *p < 0.05, **p < 0.01, ***p < 0.001 by one-way or two-way ANOVA or Student's t test. (B) n = 3–4, (D) n = 4, (E) n = 3, (F) n = 3, (G) n = 6–7, (I) n = 3, and (M) n = 3 biological replicates.
See also Figure S6.

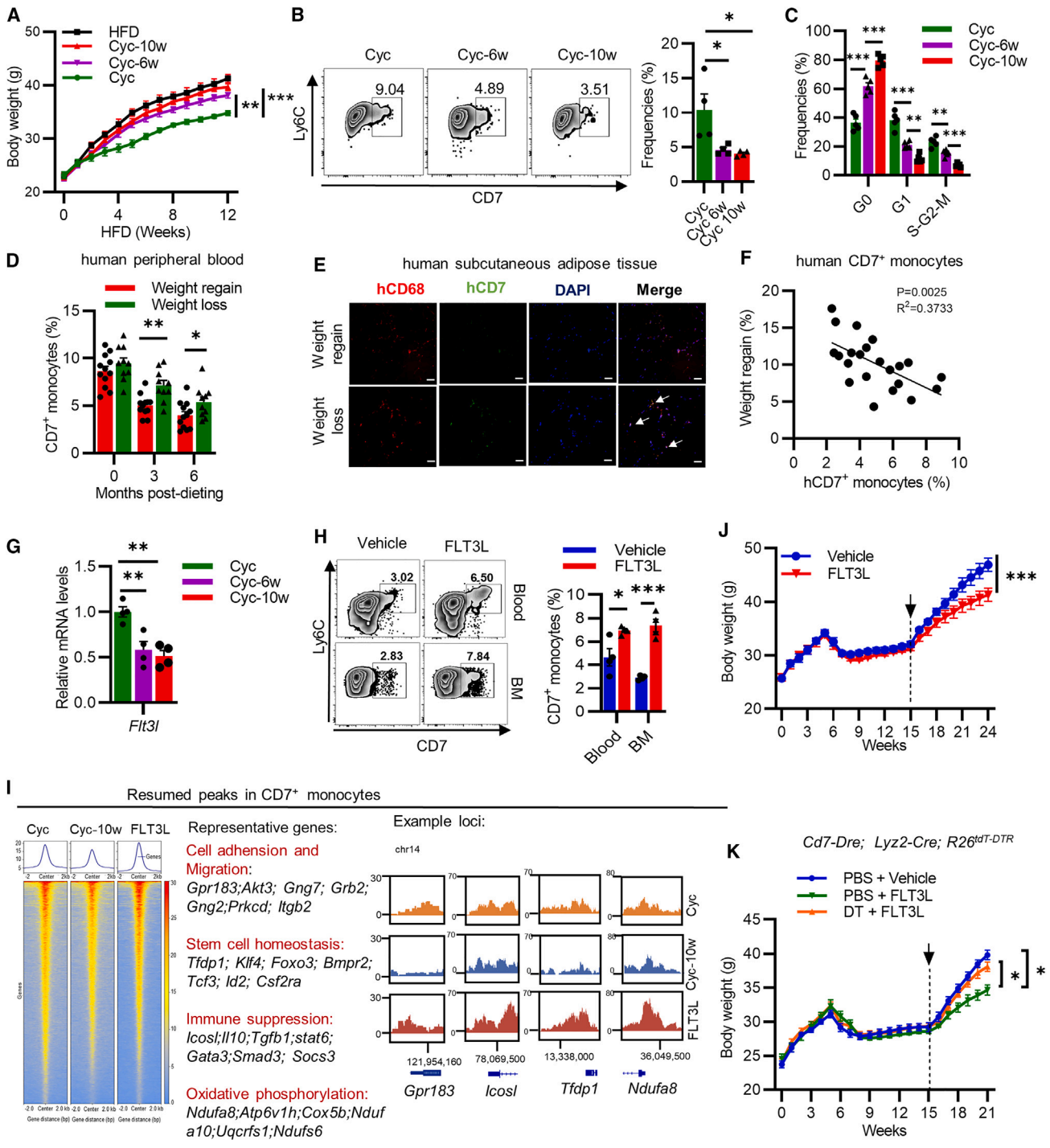

Figure 7. FLT3 ligand stimulation rejuvenates CD7$^+$ monocytes and thus inhibits weight regain

(A) The body weight curve of lethally irradiated CD45.2 WT mice transferred with the BM collected as indicated. Mice were fed an HFD after reconstitution.

(B) Flow cytometry analysis of BM CD7$^+$ monocytes from mice fed an HFD and switched to ND for 3 weeks (Cyc), 6 weeks (Cyc-6w), and 10 weeks (Cyc-10w).

(C) Cell-cycle analysis of BM CD7$^+$ monocytes.

(D) Flowcytometry analysis of human circulating CD7$^+$ monocytes from post-dieting individuals who keep weight loss or experienced weight regain after 6 months (n = 12).

(E) Representative images of co-localization of CD68 (red) and CD7 (green) in human subcutaneous adipose tissues from post-dieting individuals who keep weight loss or experienced weight regain (scale bars, 100 μm).

(F) Pearson correlation analysis between frequencies of peripheral blood hCD7$^+$ monocytes and the degree of weight regain in post-dieting individuals.

(G) Relative mRNA levels of *Flt3l* in BM cells of Cyc, Cyc-6w, and Cyc-10w mice.

(legend continued on next page)

understand the mechanisms driving recurrent weight regain have largely focused on how it is established, which can involve changes in hormone levels, extracellular matrix remodeling, and gut microbiota composition.[16,33,34] Previous studies show that obesity history induces persistent changes in circulating and visceral adipose tissue immune cell profiles even after appreciable weight loss.[12] Among the immune cell types, $CD4^+$ T cells are shown to memorize the inflammatory status of obesity and contribute to rapid weight regain.[12] Since the body has sophisticated positive and negative feedback during inflammation, it is interesting to hypothesize that different immune cells may orchestrate an integrated response to nutritional stress. Here, we found that in contrast to lymphoid $CD4^+$ T cells, BM-derived $CD7^+$ monocytes display a counter-regulatory effect on rapid weight regain.

Previous studies have demonstrated that FGL2 mediates macrophage activation and cell adhesion,[35] and it maintains the immunosuppressive activity of Tregs.[36] Here, we demonstrated that FGL2 mediates the effects of $CD7^+$ monocytes on beige fat thermogenesis. Through mass spectrum analysis, we screened out TMEM120A as the functional receptor of FGL2. The expression of *Tmem120a* was about 25% lower in subcutaneous adipose tissue of obese Arizona Pima Native Americans.[37] Besides, cold exposure promotes *Tmem120a* levels in the iWAT of mice.[38] In line with these studies, we found that knockdown of *Tmem120a* abolished the effects of FGL2 in fat thermogenesis. These results indicate that TMEM120A may be a potential target to treat obesity.

FLT3 is expressed by BM progenitors at many different stages of lymphoid and myeloid development. Treatment of mice with FLT3L is commonly adopted to expand BM DC progenitors.[32] $CD7^+$ monocytes are endowed with stem cell features and are marked by the specific expression of FLT3. We found that diverse nutritional stress in the BM niche results in the local fluctuation of *Flt3l* expression and altered $CD7^+$ monocyte proportions. FLT3L stimulation rejuvenated anti-obesity effects of $CD7^+$ monocytes, thus alleviating weight regain. Though there is a possibility that FLT3L may function via other mechanisms,[39] these results demonstrate that FLT3L stimulation at least partially regulates weight regain by expanding the pool of $CD7^+$ monocytes.

A distinguishing feature of the trained innate immune cell is its ability to mount a stronger response when rechallenged with the same pathogen or danger signal.[40] Here, a unique pool of BM $CD7^+$ monocytes was endowed with metabolic-memory capacities upon weight loss and was capable of controlling secondary overnutrition-induced obesity. Through ATAC-seq, we found that most peaks around genes related to inflammation and oxidative stress were resolved after weight loss, whereas peaks around genes showing immunosuppressive function and stem cell maintenance persistently increased. These epigenetic adaptations imprint $CD7^+$ monocytes with metabolic memories and therefore function as sentinels to counteract secondary obesity. As other innate immune cells, such as NK cells, can also develop trained immunity,[40] epigenetic rewiring that may underlie the adaptive characteristics of other innate immune cell populations during obesity awaits further investigation.

Taken together, we have found that weight loss after obesity triggers persistent epigenetic changes in chromatin regions of $CD7^+$ monocytes, leading to enhanced beige fat thermogenesis and consequently constraints in weight regain.

Limitations of the study

One limitation of this work is that we cannot exclude the possibility that other factors besides FGL2 secreted by $CD7^+$ monocytes contribute to obesity control. Moreover, follow-up work is needed to determine how $CD7^+$ monocytes sense fluctuating nutritional stress and expand upon diet switch. Finally, although we showed that $CD7^+$ monocytes negatively correlated with body weight regain in humans, whether and how $CD7^+$ monocytes would function to regulate human body weight regain remains to be further elucidated.

STAR★METHODS

Detailed methods are provided in the online version of this paper and include the following:

- KEY RESOURCES TABLE
- RESOURCE AVAILABILITY
  - Lead contact
  - Materials availability
  - Data and code availability
- EXPERIMENTAL MODEL AND SUBJECT DETAILS
  - Animal models
  - Study participants
  - Cell culture and differentiated adipocytes
- METHOD DETAILS
  - Single-cell RNA sequencing (scRNA-seq) and bioinformatics analysis
  - ATAC-Seq and bioinformatics analysis
  - Flow cytometry
  - Adoptive transfer of human $CD7^+$ monocytes
  - Bone-marrow chimeric mice construction
  - In vivo tracing of $CD7^+$ monocytes distribution
  - siRNA-mediated gene knockdown
  - Cold exposure experiment
  - Comprehensive lab animal monitoring system

(H) Flow cytometry analysis of $CD7^+$ monocytes in BM and peripheral blood from mice treated with FLT3L or vehicle.
(I) Density plots depict resume ATAC-seq peaks at summits ±2 kb in $CD7^+$ monocytes of FLT3L mice against resting Cyc-10w mice with heatmap of individual peaks beneath. Representative genes are shown (middle). The right panel is snapshots of genomic loci.
(J) The body weight curve of Cyc-10w WT mice treated with or without FLT3L as indicated.
(K) The body weight curve of Cyc-10w *Cd7-Dre; Lyz2-Cre; R26*$^{tdT\text{-}DTR}$ mice treated with or without DT and stimulated with or without FLT3L as indicated under HFD feeding.
Data are shown as the mean ± SEM. *$p < 0.05$, **$p < 0.01$, ***$p < 0.001$ by two-way ANOVA or Student's t test. (A) n = 5–7, (B) n = 4, (C) n = 5, (D) n = 12, (E) n = 3, (G) n = 4, (H) n = 4, (J) n = 5, and (K) n = 5–6 biological replicates.
See also Figure S7 and Table S1.

- Glucose tolerance test (GTT) and insulin tolerance test (ITT)
- Bone marrow monocytes and macrophages isolation
- Protein treatment
- Seahorse Cell Mito Stress Test
- Isolation of mouse and human T cells
- Co-culture experiment
- Transwell migration assay
- Pull down assay and mass spectrometry analysis
- Molecular docking analysis
- ELISA
- Co-IP and Western blot analysis
- Histochemistry, Immunohistochemistry, and Immunofluorescence
- qPCR Analysis

● QUANTIFICATION AND STATISTICAL ANALYSIS

SUPPLEMENTAL INFORMATION

Supplemental information can be found online at https://doi.org/10.1016/j.cmet.2023.08.009.

ACKNOWLEDGMENTS

This work was supported by the National Natural Science Foundation of China (grant nos. 92149306, 82120108009, 81930022, and 82170866), the China Postdoctoral Science Foundation (grant no. 2022M713514), and the Natural Science Foundation of Hunan Province, China (grant no. 2022JJ30990). We thank Prof. Hongbo He, Prof. Wenfeng Xiao, Prof. Hongqi Zhang, and Prof. Qile Gao (Xiangya Hospital of Central South University) for their help in collecting the human bone marrow samples. We thank Prof. Yong-Jun Zheng (the First Affiliated Hospital of Naval Medical University) for helping with scRNA-seq analysis and Prof. Bing Sun (Shanghai Institute of Biochemistry and Cell Biology, Chinese Academy of Sciences) for offering the CD45.1 mice.

AUTHOR CONTRIBUTIONS

X.-H.L. and H.-Y.Z. designed and supervised the experiments. H.-Y.Z. analyzed the results and drafted the manuscript. H.-Y.Z. and X.F. carried out most of the experiments. L.-W.W. and R.Z. helped conduct animal experiments. R.-B.L. and Y.H. helped to analyze single-cell RNA-seq data. Q.G., H.S., and X.C. helped collect and analyze the human samples.

DECLARATION OF INTERESTS

The authors declare no competing interests.

Received: March 1, 2023
Revised: June 19, 2023
Accepted: August 18, 2023
Published: September 12, 2023

REFERENCES

1. Kelly, T., Yang, W., Chen, C.S., Reynolds, K., and He, J. (2008). Global burden of obesity in 2005 and projections to 2030. Int. J. Obes. (Lond) *32*, 1431–1437. https://doi.org/10.1038/ijo.2008.102.
2. Chew, N.W.S., Ng, C.H., Tan, D.J.H., Kong, G., Lin, C., Chin, Y.H., Lim, W.H., Huang, D.Q., Quek, J., Fu, C.E., et al. (2023). The global burden of metabolic disease: data from 2000 to 2019. Cell Metab. *35*, 414–428.e3. https://doi.org/10.1016/j.cmet.2023.02.003.
3. Look AHEAD Research Group (2014). Eight-year weight losses with an intensive lifestyle intervention: the look AHEAD study. Obesity (Silver Spring) *22*, 5–13. https://doi.org/10.1002/oby.20662.
4. Iepsen, E.W., Lundgren, J., Dirksen, C., Jensen, J.E., Pedersen, O., Hansen, T., Madsbad, S., Holst, J.J., and Torekov, S.S. (2015). Treatment with a GLP-1 receptor agonist diminishes the decrease in free plasma leptin during maintenance of weight loss. Int. J. Obes. (Lond) *39*, 834–841. https://doi.org/10.1038/ijo.2014.177.
5. Shah, M., Simha, V., and Garg, A. (2006). Review: long-term impact of bariatric surgery on body weight, comorbidities, and nutritional status. J. Clin. Endocrinol. Metab. *91*, 4223–4231. https://doi.org/10.1210/jc.2006-0557.
6. Haganes, K.L., Silva, C.P., Eyjólfsdóttir, S.K., Steen, S., Grindberg, M., Lydersen, S., Hawley, J.A., and Moholdt, T. (2022). Time-restricted eating and exercise training improve HbA1c and body composition in women with overweight/obesity: a randomized controlled trial. Cell Metab. *34*, 1457–1471.e4. https://doi.org/10.1016/j.cmet.2022.09.003.
7. Yamada, T., Hara, K., Svensson, A.K., Shojima, N., Hosoe, J., Iwasaki, M., Yamauchi, T., and Kadowaki, T. (2015). Successfully achieving target weight loss influences subsequent maintenance of lower weight and dropout from treatment. Obesity (Silver Spring) *23*, 183–191. https://doi.org/10.1002/oby.20874.
8. Bray, G.A., Frühbeck, G., Ryan, D.H., and Wilding, J.P.H. (2016). Management of obesity. Lancet *387*, 1947–1956. https://doi.org/10.1016/S0140-6736(16)00271-3.
9. Diabetes; Prevention Program Research Group, Knowler, W.C., Fowler, S.E., Hamman, R.F., Christophi, C.A., Hoffman, H.J., Brenneman, A.T., Brown-Friday, J.O., Goldberg, R., et al. (2009). 10-year follow-up of diabetes incidence and weight loss in the Diabetes Prevention Program Outcomes Study. Lancet *374*, 1677–1686. https://doi.org/10.1016/S0140-6736(09)61457-4.
10. Grzelka, K., Wilhelms, H., Dodt, S., Dreisow, M.L., Madara, J.C., Walker, S.J., Wu, C., Wang, D., Lowell, B.B., and Fenselau, H. (2023). A synaptic amplifier of hunger for regaining body weight in the hypothalamus. Cell Metab. *35*, 770–785.e5. https://doi.org/10.1016/j.cmet.2023.03.002.
11. Anderson, E.K., Gutierrez, D.A., Kennedy, A., and Hasty, A.H. (2013). Weight cycling increases T-cell accumulation in adipose tissue and impairs systemic glucose tolerance. Diabetes *62*, 3180–3188. https://doi.org/10.2337/db12-1076.
12. Zou, J., Lai, B., Zheng, M., Chen, Q., Jiang, S., Song, A., Huang, Z., Shi, P., Tu, X., Wang, D., et al. (2018). CD4+ T cells memorize obesity and promote weight regain. Cell. Mol. Immunol. *15*, 630–639. https://doi.org/10.1038/cmi.2017.36.
13. Sumithran, P., Prendergast, L.A., Delbridge, E., Purcell, K., Shulkes, A., Kriketos, A., and Proietto, J. (2011). Long-term persistence of hormonal adaptations to weight loss. N. Engl. J. Med. *365*, 1597–1604. https://doi.org/10.1056/NEJMoa1105816.
14. Maclean, P.S., Bergouignan, A., Cornier, M.A., and Jackman, M.R. (2011). Biology's response to dieting: the impetus for weight regain. Am. J. Physiol. Regul. Integr. Comp. Physiol. *301*, R581–R600. https://doi.org/10.1152/ajpregu.00755.2010.
15. Ebbeling, C.B., Swain, J.F., Feldman, H.A., Wong, W.W., Hachey, D.L., Garcia-Lago, E., and Ludwig, D.S. (2012). Effects of dietary composition on energy expenditure during weight-loss maintenance. JAMA *307*, 2627–2634. https://doi.org/10.1001/jama.2012.6607.
16. Thaiss, C.A., Itav, S., Rothschild, D., Meijer, M.T., Levy, M., Moresi, C., Dohnalová, L., Braverman, S., Rozin, S., Malitsky, S., et al. (2016). Persistent microbiome alterations modulate the rate of post-dieting weight regain. Nature *540*, 544–551. https://doi.org/10.1038/nature20796.
17. Benova, A., and Tencerova, M. (2020). Obesity-induced changes in bone marrow homeostasis. Front. Endocrinol. (Lausanne) *11*, 294. https://doi.org/10.3389/fendo.2020.00294.
18. Zhou, H., Peng, X., Hu, J., Wang, L., Luo, H., Zhang, J., Zhang, Y., Li, G., Ji, Y., Zhang, J., et al. (2021). DsbA-L deficiency in T cells promotes diet-induced thermogenesis through suppressing IFN-γ production. Nat. Commun. *12*, 326. https://doi.org/10.1038/s41467-020-20665-4.
19. Gatto, D., Wood, K., Caminschi, I., Murphy-Durland, D., Schofield, P., Christ, D., Karupiah, G., and Brink, R. (2013). The chemotactic receptor EBI2 regulates the homeostasis, localization and immunological function

of splenic dendritic cells. Nat. Immunol. *14*, 446–453. https://doi.org/10.1038/ni.2555.

20. Liu, C., Yang, X.V., Wu, J., Kuei, C., Mani, N.S., Zhang, L., Yu, J., Sutton, S.W., Qin, N., Banie, H., et al. (2011). Oxysterols direct B-cell migration through EBI2. Nature *475*, 519–523. https://doi.org/10.1038/nature10226.
21. Chalmin, F., Rochemont, V., Lippens, C., Clottu, A., Sailer, A.W., Merkler, D., Hugues, S., and Pot, C. (2015). Oxysterols regulate encephalitogenic CD4(+) T cell trafficking during central nervous system autoimmunity. J. Autoimmun. *56*, 45–55. https://doi.org/10.1016/j.jaut.2014.10.001.
22. Hannedouche, S., Zhang, J., Yi, T., Shen, W., Nguyen, D., Pereira, J.P., Guerini, D., Baumgarten, B.U., Roggo, S., Wen, B., et al. (2011). Oxysterols direct immune cell migration via EBI2. Nature *475*, 524–527. https://doi.org/10.1038/nature10280.
23. Min, S.Y., Kady, J., Nam, M., Rojas-Rodriguez, R., Berkenwald, A., Kim, J.H., Noh, H.L., Kim, J.K., Cooper, M.P., Fitzgibbons, T., et al. (2016). Human 'brite/beige' adipocytes develop from capillary networks, and their implantation improves metabolic homeostasis in mice. Nat. Med. *22*, 312–318. https://doi.org/10.1038/nm.4031.
24. Bekkering, S., Domínguez-Andrés, J., Joosten, L.A.B., Riksen, N.P., and Netea, M.G. (2021). Trained immunity: reprogramming innate immunity in health and disease. Annu. Rev. Immunol. *39*, 667–693. https://doi.org/10.1146/annurev-immunol-102119-073855.
25. Gourbal, B., Pinaud, S., Beckers, G.J.M., Van Der Meer, J.W.M., Conrath, U., and Netea, M.G. (2018). Innate immune memory: an evolutionary perspective. Immunol. Rev. *283*, 21–40. https://doi.org/10.1111/imr.12647.
26. Fontenot, J.D., Rasmussen, J.P., Williams, L.M., Dooley, J.L., Farr, A.G., and Rudensky, A.Y. (2005). Regulatory T cell lineage specification by the forkhead transcription factor foxp3. Immunity *22*, 329–341. https://doi.org/10.1016/j.immuni.2005.01.016.
27. Czapiewski, R., Batrakou, D.G., de Las Heras, J.I., Carter, R.N., Sivakumar, A., Sliwinska, M., Dixon, C.R., Webb, S., Lattanzi, G., Morton, N.M., et al. (2022). Genomic loci mispositioning in Tmem120a knockout mice yields latent lipodystrophy. Nat. Commun. *13*, 321. https://doi.org/10.1038/s41467-021-27869-2.
28. Larsen, S.B., Cowley, C.J., Sajjath, S.M., Barrows, D., Yang, Y., Carroll, T.S., and Fuchs, E. (2021). Establishment, maintenance, and recall of inflammatory memory. Cell Stem Cell *28*, 1758–1774.e8. https://doi.org/10.1016/j.stem.2021.07.001.
29. Netea, M.G., and van der Meer, J.W. (2017). Trained immunity: an ancient way of remembering. Cell Host Microbe *21*, 297–300. https://doi.org/10.1016/j.chom.2017.02.003.
30. Iwamura, C., Bouladoux, N., Belkaid, Y., Sher, A., and Jankovic, D. (2017). Sensing of the microbiota by NOD1 in mesenchymal stromal cells regulates murine hematopoiesis. Blood *129*, 171–176. https://doi.org/10.1182/blood-2016-06-723742.
31. Kim, E.H., and Suresh, M. (2013). Role of PI3K/Akt signaling in memory CD8 T cell differentiation. Front. Immunol. *4*, 20. https://doi.org/10.3389/fimmu.2013.00020.
32. Hernández-García, E., Cueto, F.J., Cook, E.C.L., Redondo-Urzainqui, A., Charro-Zanca, S., Robles-Vera, I., Conde-Garrosa, R., Nikolić, I., Sabio, G., Sancho, D., et al. (2022). Conventional type 1 dendritic cells protect against age-related adipose tissue dysfunction and obesity. Cell. Mol. Immunol. *19*, 260–275. https://doi.org/10.1038/s41423-021-00812-7.
33. van Baak, M.A., and Mariman, E.C.M. (2019). Mechanisms of weight regain after weight loss - the role of adipose tissue. Nat. Rev. Endocrinol. *15*, 274–287. https://doi.org/10.1038/s41574-018-0148-4.
34. Zhong, W., Wang, H., Yang, Y., Zhang, Y., Lai, H., Cheng, Y., Yu, H., Feng, N., Huang, R., Liu, S., et al. (2022). High-protein diet prevents fat mass increase after dieting by counteracting Lactobacillus-enhanced lipid absorption. Nat. Metab. *4*, 1713–1731. https://doi.org/10.1038/s42255-022-00687-6.
35. Liu, Y., Xu, S., Xiao, F., Xiong, Y., Wang, X., Gao, S., Yan, W., and Ning, Q. (2010). The FGL2/fibroleukin prothrombinase is involved in alveolar macrophage activation in COPD through the MAPK pathway. Biochem. Biophys. Res. Commun. *396*, 555–561. https://doi.org/10.1016/j.bbrc.2010.04.145.
36. Joller, N., Lozano, E., Burkett, P.R., Patel, B., Xiao, S., Zhu, C., Xia, J., Tan, T.G., Sefik, E., Yajnik, V., et al. (2014). Treg cells expressing the coinhibitory molecule TIGIT selectively inhibit proinflammatory Th1 and Th17 cell responses. Immunity *40*, 569–581. https://doi.org/10.1016/j.immuni.2014.02.012.
37. Lee, Y.H., Nair, S., Rousseau, E., Allison, D.B., Page, G.P., Tataranni, P.A., Bogardus, C., and Permana, P.A. (2005). Microarray profiling of isolated abdominal subcutaneous adipocytes from obese vs non-obese Pima Indians: increased expression of inflammation-related genes. Diabetologia *48*, 1776–1783. https://doi.org/10.1007/s00125-005-1867-3.
38. Rosell, M., Kaforou, M., Frontini, A., Okolo, A., Chan, Y.W., Nikolopoulou, E., Millership, S., Fenech, M.E., MacIntyre, D., Turner, J.O., et al. (2014). Brown and white adipose tissues: intrinsic differences in gene expression and response to cold exposure in mice. Am. J. Physiol. Endocrinol. Metab. *306*, E945–E964. https://doi.org/10.1152/ajpendo.00473.2013.
39. Cueto, F.J., and Sancho, D. (2021). The Flt3L/Flt3 axis in dendritic cell biology and cancer immunotherapy. Cancers (Basel) *13*. https://doi.org/10.3390/cancers13071525.
40. Netea, M.G., Joosten, L.A., Latz, E., Mills, K.H., Natoli, G., Stunnenberg, H.G., O'Neill, L.A., and Xavier, R.J. (2016). Trained immunity: a program of innate immune memory in health and disease. Science *352*, aaf1098. https://doi.org/10.1126/science.aaf1098.
41. Feng, X., Wang, L., Zhou, R., Zhou, R., Chen, L., Peng, H., Huang, Y., Guo, Q., Luo, X., and Zhou, H. (2023). Senescent immune cells accumulation promotes brown adipose tissue dysfunction during aging. Nat. Commun. *14*, 3208. https://doi.org/10.1038/s41467-023-38842-6.
42. Peng, H., Hu, B., Xie, L.Q., Su, T., Li, C.J., Liu, Y., Yang, M., Xiao, Y., Feng, X., Zhou, R., et al. (2022). A mechanosensitive lipolytic factor in the bone marrow promotes osteogenesis and lymphopoiesis. Cell Metab. *34*, 1168–1182.e6. https://doi.org/10.1016/j.cmet.2022.05.009.
43. Katchalski-Katzir, E., Shariv, I., Eisenstein, M., Friesem, A.A., Aflalo, C., and Vakser, I.A. (1992). Molecular surface recognition: determination of geometric fit between proteins and their ligands by correlation techniques. Proc. Natl. Acad. Sci. USA *89*, 2195–2199. https://doi.org/10.1073/pnas.89.6.2195.
44. Vakser, I.A. (1996). Long-distance potentials: an approach to the multiple-minima problem in ligand-receptor interaction. Protein Eng. *9*, 37–41. https://doi.org/10.1093/protein/9.1.37.
45. Morris, G.M., Huey, R., and Olson, A.J. (2008). Using AutoDock for ligand-receptor docking. Curr. Protoc. Bioinformatics *Chapter 8*. Unit 8.14. https://doi.org/10.1002/0471250953.bi0814s24.
46. Li, C.J., Xiao, Y., Sun, Y.C., He, W.Z., Liu, L., Huang, M., He, C., Huang, M., Chen, K.X., Hou, J., et al. (2021). Senescent immune cells release grancalcin to promote skeletal aging. Cell Metab. *33*, 1957–1973.e6. https://doi.org/10.1016/j.cmet.2021.08.009.
47. Feng, X., Xiao, Y., He, J., Yang, M., Guo, Q., Su, T., Huang, Y., Yi, J., Li, C.J., Luo, X.H., et al. (2022). Long noncoding RNA Gm31629 protects against mucosal damage in experimental colitis via YB-1/E2F pathway. JCI Insight *7*. https://doi.org/10.1172/jci.insight.150091.
48. Feng, X., Xiao, Y., Guo, Q., Peng, H., Zhou, H.Y., Wang, J.P., and Xia, Z.Y. (2022). Parathyroid hormone alleviates non-alcoholic liver steatosis via activating the hepatic cAMP/PKA/CREB pathway. Front. Endocrinol. (Lausanne) *13*, 899731. https://doi.org/10.3389/fendo.2022.899731.
49. Mina, A.I., LeClair, R.A., LeClair, K.B., Cohen, D.E., Lantier, L., and Banks, A.S. (2018). CalR: a web-based analysis tool for indirect calorimetry experiments. Cell Metab. *28*, 656–666.e1. https://doi.org/10.1016/j.cmet.2018.06.019.

STAR★METHODS

KEY RESOURCES TABLE

REAGENT or RESOURCE	SOURCE	IDENTIFIER
Antibodies		
Anti-UCP1	Abcam	Cat# ab10983; RRID: AB_2241462
Anti-PGC-1α	Santa Cruz Biotechnology	Cat# Sc-517380; RRID: AB_2755043
Anti-cAMP	Abcam	Cat#ab76238; RRID: AB_1523259
Anti-phospho-CREB (Ser133)	Cell Signaling Technology	Cat#9198; RRID: AB_2561044
Anti-CREB1	Proteintech	Cat# 12208-1-AP; RRID: AB_2245417
Anti-phospho-(Ser/Thr) PKA Substrate	Cell Signaling Technology	Cat# 9621; RRID: AB_330304
Anti-β Actin	Proteintech	Cat#66009-1-Ig; RRID: AB_2687938
Anti-α Tubulin	Proteintech	Cat# 11224-1-AP; RRID: AB_2210206
Anti-FGL2	Proteintech	Cat# 11827–1-AP; RRID: AB_2103947
Anti-GAPDH	OriGene	Cat# TA802519; RRID: AB_2626378
Anti-His Tag	Cell Signaling Technology	Cat# 2366; RRID: AB_2115719
Anti-TMEM120A	Proteintech	Cat# 17455-1-AP; RRID: AB_2204630
Anti-HA Tag	Cell Signaling Technology	Cat# 3724; RRID: AB_1549585
Anti-DYKDDDDK Tag	Cell Signaling Technology	Cat# 14793; RRID: AB_2572291
Anti-DDK (FLAG)	OriGene	Cat# TA50011; RRID: AB_2622345
Anti-HA Tag	Abmart	Cat#M20003; RRID: AB_2864345
Anti-CD7	Proteintech	Cat# 60209-1-Ig; RRID: AB_10953398
Biotin-Flt3	BioLegend	Cat# 135307; RRID: AB_1953266
Alexa fluor 488 anti-mouse IgG	Invitrogen	Cat# A-10680; RRID: AB_2534062
Alexa fluor 647 anti-rabbit IgG	Invitrogen	Cat# A32795TR; RRID: AB_2866496
Anti-Ki67	Proteintech	Cat#27309-1-AP; RRID: AB_2756525
BV510 anti-mouse CD45.1	BioLegend	Cat# 110741; RRID: AB_2563378
APC/Cyanine7 anti-mouse CD45.2	BioLegend	Cat# 109824; RRID: AB_830789
BV510 anti-mouse/human CD11b	BioLegend	Cat# 101263; RRID: AB_2629529
PE anti-mouse Ly6G	BioLegend	Cat# 127607; RRID: AB_1186104
PE/Cy7 anti-mouse Ly6C	BioLegend	Cat# 128018; RRID: AB_1732082
Percp/Cy5.5-Streptavidin	BioLegend	Cat# 405214; RRID: AB_2716577
Anti-GPR183	Alomone labs	Cat# AGR-063; RRID: AB_2925069
PE anti-human FLT3	BioLegend	Cat# 313306; RRID: AB_314991
APC anti-human CD4	BioLegend	Cat# 300514; RRID: AB_314082
APC/Cy7-mouse anti human CD3	BD Bioscience	Cat# 557832; RRID: AB_396890
Percp anti-human CD14	BioLegend	Cat# 325632; RRID: AB_2563328
PerCP/Cyanine5.5 anti-mouse CD3	BioLegend	Cat# 100218; RRID: AB_1595492
FITC anti-mouse CD4	BioLegend	Cat# 100406; RRID: AB_312691
Brilliant Violet 421 anti-mouse CD19	BioLegend	Cat# 115549; RRID: AB_2563066
PE anti-mouse FOXP3	BioLegend	Cat# 118904; RRID: AB_2936574
APC anti-mouse NK-1.1	BioLegend	Cat# 108710; RRID: AB_313397
APC/Cyanine7 anti-mouse CD8a	Biolegend	Cat# 100713; RRID: AB_312752
Pacific Blue anti-mouse CD86	Biolegend	Cat# 105022; RRID: AB_493466
Alexa fluor 488 anti-mouse/human GL7 antigen	Biolegend	Cat# 144612; RRID: AB_2563285
PE/Cyanine7 anti-mouse CD69	Biolegend	Cat# 104512; RRID: AB_493564
APC anti-mouse/human CD44	Biolegend	Cat#103011; RRID: AB_312962
APC/Cyanine7 anti-mouse Ly6G	Biolegend	Cat# 127624; RRID: AB_10640819

(*Continued on next page*)

Continued

REAGENT or RESOURCE	SOURCE	IDENTIFIER
Anti-human CD68	Servicebio	Cat# GB113150; RRID: AB_2924885
Biological samples		
Human bone marrow	Xiangya Hospital of Central South University	N/A
Chemicals, peptides, and recombinant proteins		
Recombinant Mouse FGL2 Protein	MedChem Express	Cat#HY-P700990
Recombinant Mouse Flt3 Ligand Protein	SinoBiological	Cat#51113-M02H
Diphtheria Toxin	Sigma	Cat#D0564
FCCP	Sigma	Cat#C2920
Oligmycin A	GlpBio	Cat#GC16859
Antimycin A	GlpBio	Cat#GC49360
Rotenone	Sigma	Cat#45656
Fetal bovine serum	Gibco	Cat#10091-148
3-isobutyl-1-methylxanthine	Sigma	Cat#I5879
Dexamethasone	Sigma	Cat#D4902
Insulin	Sigma	Cat#91077C
Indomethacin	Sigma	Cat#I7378
Rosiglitazone	MedChem Express	Cat#HY-17386
Triiodothyronine	MedChem Express	Cat#HY-A0070A
7α,25-Dihydroxycholesterol	MedChem Express	Cat#HY-113962
H89	Selleck	Cat#S1582
DAPI	Solarbio	Cat#C0060
M-CSF	Proteintech	Cat#HZ-1192
Critical commercial assays		
Mouse FGL2 ELISA Kit	Abcam	Cat#ab283884
Mose AGRP ELISA Kit	Jingmei Biotechnology	Cat#J43266-A
Mouse Grelin ELISA Kit	Jingmei Biotechnology	Cat#J43261-A
Mouse NPY ELISA Kit	Jingmei Biotechnology	Cat#J2501-A
Mouse Leptin ELISAKIT	4A Biotech	Cat#CME0061
Mouse TNF-α ELISA Kit	4A Biotech	Cat#CME0004
Mouse IFN-γ ELISA Kit	4A Biotech	Cat#CME0003
Human TNF-α ELISA Kit	4A Biotech	Cat#CHE0019
Human IFN-γ ELISA Kit	4A Biotech	Cat#CHE0017
Zombie NIR Fixable Viability Kit	Biolegend	Cat#423106
Zombie Aqua Fixable Viability Kit	Biolegend	Cat#423102
Membrane protein extraction kit	Beyotime	Cat#P0033
BCA Protein Colorimetric Assay Kit	Elabscience	Cat#E-BC-K318-M
Deposited data		
scRNA-seq data for mice	This paper	SRA: PRJNA957492
scRNA-seq data for human	This paper	GSA-Human: HRA006912
ATAC-Seq data	This paper	SRA: PRJNA957492
Mass spectrometry data	This paper	ProteomeXchange Consortium: PXD043231
Original western blot images and all raw data	This paper	Data S1
Experimental models: Cell lines		
HEK293T	ATCC	CRL-3216
C3H10T1/2	Procell	CL-0325

(*Continued on next page*)

Continued

REAGENT or RESOURCE	SOURCE	IDENTIFIER
Experimental models: Organisms/strains		
C57/BL6J mice	Hunan SJA Laboratory Animal Company. China	N/A
CD45.1 mice	Shanghai Institute of Biochemistry and Cell Biology	N/A
NSG mice	Shanghai Model Organisms Center China	NOD.Cg-*Prkdc*^{scid}*Il2rg*^{em1Smoc}
R26$^{CAG\text{-}LSL\text{-}RSR\text{-}tdTomato\text{-}2A\text{-}DTR}$	Shanghai Model Organisms Center China	C57BL/6JSmoc-*Gt(ROSA) 26Sor*$^{em1(CAG\text{-}LSL\text{-}RSR\text{-}tdTomato\text{-}2A\text{-}DTR)Smoc}$
Lyz2-Cre mice	Cyagen Biosciences China	004781-B6.129P2-Lyz2$^{tm1(cre)Ifo}$/J
Cd7-Dre	This paper	N/A
Fgl2 floxed mice	Cyagen Biosciences China	C57BL/6J-Fgl2^{em1Cflox}/Cya
Oligonucleotides		
siRNA targeting sequence: si-m-Tmem120a: TCACCATCATCCTCATCGT	This paper	N/A
siRNA targeting sequence: si-m-Fgl2: GGGCAACGATAAAATTCAT	This paper	N/A
siRNA targeting sequence: si-m-Gpr183: CAACCACTCTCTATTCAAT	This paper	N/A
See Table S2 for qPCR primers	This paper	N/A
Recombinant DNA		
HA-TMEM120A plasmid	This paper	N/A
His-FGL2 plasmid	This paper	N/A
Flag-FGL2 plasmid	This paper	N/A
Flag-FGL2 Δ1-70 plasmid	This paper	N/A
Flag-FGL2 Δ71-157 plasmid	This paper	N/A
Flag-FGL2 Δ100-122 plasmid	This paper	N/A
Flag-FGL2 Δ197-429 plasmid	This paper	N/A
Software and algorithms		
ImageJ	NIH	https://imagej.nih.gov/ij/
Wave Desktop	Agilent	https://www.agilent.com/en/products/cell-analysis/cell-analysis-software#0
FlowJo V10	FlowJo	https://www.flowjo.com/solutions/flowjo
GraphPad Prism 8 software	GraphPad Software	https://www.graphpad.com/
CLAX	Columbus Instruments	https://clax.software.informer.com/
PyMOL	N/A	http://www.pymol.org/pymol.
Other		
Seahorse XFe96 Analyzers	Agilent	N/A
BD FACSAria III	BD Biosciences	N/A
BD FACSCanto II	BD Biosciences	N/A

RESOURCE AVAILABILITY

Lead contact

Further information and requests for resources and reagents should be directed to and will be fulfilled by the Lead Contact, XiangHang Luo (xianghangluo@csu.edu.cn).

Materials availability

All the data and materials that support the findings of this study are available within the article and supplemental information or available from the authors upon request.

Data and code availability

- The scRNA-seq data and ATAC-Seq data from mouse samples produced in this paper have been deposited in the Sequence Read Archive database under accession number: PRJNA957492.
- The scRNA-seq data from human samples produced in this paper have been deposited in the Genome Sequence Archive (GSA) for human under accession number: HRA004840.
- The mass spectrometry proteomics data have been deposited to the ProteomeXchange Consortium via the PRIDE partner repository with the dataset identifier PXD043231.
- The data for Genotype Tissue Expression (GTEx) database are acquired from GEPIA2 (http://gepia2.cancer-pku.cn/).
- Original western blot images and all raw data used to create the graphs can be found in Data S1.
- This paper does not report original code.

EXPERIMENTAL MODEL AND SUBJECT DETAILS

Animal models

We obtained *Lyz2-Cre* mice, *Fgl2*$^{f/f}$ mice from Cyagen (China) and R26$^{CAG\text{-}LSL\text{-}RSR\text{-}tdTomato\text{-}2A\text{-}DTR}$ mice from Shanghai Model Organisms Center (China), respectively. The *Cd7-Dre* mice were constructed by CRISPR/Cas9-mediated Dre sequence knocking into the endogenous *Cd7* gene locus in Cyagen (China). *Cd7-Dre;Lyz2-Cre;R26*$^{tdT\text{-}DTR}$ mice were generated by crossing *R26*$^{CAG\text{-}LSL\text{-}RSR\text{-}tdTomato\text{-}2A\text{-}DTR}$ mice with *Lyz2-Cre* and *Cd7-Dre* mice to excise the stop cassette flanked by loxP and rox recombination sites, respectively, allowing tracing of Lyz2$^+$Cd7$^+$ cell population and diphtheria toxin (DT)-mediated conditional cell knockout. For Lyz2$^+$CD7$^+$ cell population ablation, *Cd7-Dre;Lyz2-Cre;R26*$^{tdT\text{-}DTR}$ mice were injected intraperitoneally with 15 ng/g DT (Sigma) every three days. C57BL/6J wild-type mice and NOD.Cg-*Prkdc*^{scid}*Il2rg*^{em1Smoc} (NSG) mice were provided by Hunan SJA Laboratory Animal Company (China) and Shanghai Model Organisms Center (China), respectively. When applicable, mice were fed HFD for 5 weeks to induce obesity, followed by either HFD feeding for another 3 weeks (HFD group) or switched to a ND for 3 weeks to lose weight (Cyc group). All mice were kept in the specific pathogen-free facility of the Laboratory Animal Research Center of Central South University at 22-24°C except otherwise indicated with a 12 h dark/light cycle, and with ad libitum access to a regular chow diet and water. In this study, only male mice were used and all controls were age-matched as indicated in Figure legends. All animal care protocols and experiments were approved by the Institutional Animal Care and Use Committee of the Laboratory Animal Research Center of Central South University.

Study participants

Human blood samples were collected from both male and female individuals who were lean (18 < BMI < 24), obese (BMI > 30) or post-dieting (BMI < 30). The post-dieting individuals refer to people who used to be obese and succeeded in more than 10% weight loss through dieting within past six months. Detailed clinical information are provided in Table S1. For sRNA-seq, human bone marrow samples were obtained from male participants by bone marrow aspiration. The bone marrow aspiration and collection were conducted in Xiangya Hospital of Central South University. A total of 67 participants (40 males and 27 females; age range 20-45 years) were selected on the basis of the inclusion and exclusion criteria. All participants were screened using a detailed questionnaire, disease history, and physical examination. Participants with diseases of the kidney, liver, parathyroid, thyroid, diabetes mellitus, rheumatoid arthritis, ankylosing spondylitis, malabsorption syndromes, malignant tumors, hematologic diseases, alcohol, drugs or tobacco addiction, or previous pathological fractures within 1 year were excluded from the study. Participants received treatment with glucocorticoids, estrogens, thyroid hormone, parathyroid hormone, fluoride, bisphosphonate, calcitonin, thiazide diuretics, barbiturates, or antiseizure medication were also excluded. The clinical study was approved by the Ethics Committee of Xiangya Hospital of Central South University, and written informed consent was obtained from all participants before collection of BM or peripheral whole blood samples.

Cell culture and differentiated adipocytes

All cells were grown at 37°C in a 5% CO2 humid atmosphere. C3H10T1/2 preadipocytes (Procell) were cultured and induced to adipogenic differentiation as previously described.[41] In brief, confluent C3H10T1/2 preadipocytes were treated with differentiation medium supplemented with 0.5 mM 3-isobutyl-1-methylxanthine (Sigma), 1 μM dexamethasone (Sigma), 850 nM insulin (Sigma), 1 nM triiodothyronine (MedChem Express), 125 nm indomethacin (Sigma) and 1 μM rosiglitazone (MedChem Express) for 2 days and subsequently cultured in maintaining medium supplemented with 1 nM triiodothyronine, 850 nM insulin, and 1 μM rosiglitazone for another 2 days. Differentiated adipocytes at day 4 were cultured in complete medium until used for experiments.

METHOD DETAILS

Single-cell RNA sequencing (scRNA-seq) and bioinformatics analysis

BM immune cells from ND, HFD, and Cyc mice were flushed using ice-cold α-MEM, then dispelled into single cells for further scRNA-seq conducted by OE Biotech (Shanghai, China). The scRNA-seq library was constructed using a 10X Genomics Chromium Single Cell 30 Reagent Kit v3 according to the user guide. The procedure samples a pool of ~3,500,000 10x Barcodes, and thousands of cells are partitioned into nanoliter-scale Gel Beads-in-emulsion (GEMs), where all generated cDNA shares a common 10x Barcode,

thus separately indexing each cell's transcriptome. Libraries were sequenced and 10x Barcodes are used to associate individual reads back to the individual partitions. The 10X genomics raw data were processed using the Cell Ranger software pipeline (version 5.0.0) with default parameters and produced a matrix of gene counts versus cells. The R package Seurat (version 3.1.1) was used to process the unique molecular identifier (UMI) count matrix. Quality control was processed by filtering out these cells: 1) gene numbers less than 200, UMI less than 1000 and log10GenesPerUMI less than 0.7; 2)>10% of the counts belonged to mitochondrial genes and >5% of the counts belonged to hemoglobin genes. After filtering, we used functions from Seurat for downstream analysis. All gene expression was normalized and scaled using NormalizeData and ScaleData functions. Top variable genes were identified by FindVariableGenes function for PCA analysis. Cells were clustered using the FindClusters function and visualized using a 2-dimensional Uniform Manifold Approximation and Projection (UMAP) algorithm with the Run UMAP function. We used the FindAllMarkers function to identify marker genes of each cluster. Then, we used the R package SingleR to infer the cell of origin of each of the single cells independently and identify cell types. To assign the cell type to each cluster, we scored each cluster by the normalized expressions of the following canonical markers: B cells (Cd79b, Cd19), Basophils (Ms4a2, Cd63), Common lymphoid progenitors (CLP)(Kit, Ly6a, Il7r, Flt3), Common myeloid progenitors (CMP)(Cd34, Cd16, Cd32), Dendritic cells (Cd74, Irf8), Erythroid cells (Hba-a1, Hbb-bs), Late pro-B cell (Dntt, Rag1, Cd79b, Cd19), Monocytes/Macrophages (S100a4, Ccl9, Cd300e, Cd68), Multipotent progenitor 4 (MPP4)(Cd48, Cd150), MSCs (Lepr, Cxcl12, Kitl, Angpt1), Neutrophils (Lcn2, Camp, Retnlg, Csf3r), T cells (Klrd1, Cd4, CD3d, Cd3g, Cd3e, Cd8a), NK cells (Klrd1, Trdc, Cd160, Nkg7), Plasma cells (Cd79b, Jchain, Mzb1), Pro-B cells (Cd19, Cd79b, Ezh2), Pro-Erythroid cells (Tfrc, Mki67), Pro-Neutrophils (Prtn3, Kit, Mpo, ELane). Differentially expressed genes (DEGs) were identified using the FindMarkers function. P value < 0.05 and |log2foldchange| > 0.58 was set as the threshold for significantly differential expression. Dot plots and violin plots displaying the gene expression were generated by DotPlot/Vlnplot function. Within the monocytes/macrophages cluster, cells were subclustered in the same workflow. We then performed the pseudotime-trajectory analysis for monocytes/macrophages subclusters using Monocle2. The positive significant cluster marker genes were used to sort cells in a temporal differentiation order. Dimension reduction was performed using DDRTree from Monocle2. Gene set variation analysis (GSVA) was performed using the GSVA R package to assess the gene set activity among clusters. We performed single-cell regulatory network inference and clustering (SCENIC) for monocytes/macrophage subclusters. The regulon specificity score (RSS) was calculated to identify cell type-specific regulatory network.

For scRNA-seq of human BM samples, BM cells were processed in the same procedure to acquire the 10X genomics raw data, and to proceed with the following bioinformatics analysis. Specially, we scored each cluster by the normalized expressions of the following canonical markers for cell type clustering: B cells (CD19, CD79B), Dendritic cells (CD74, IRF8), Erythroblast (HBB, TFRC), GMP (ELANE, MPO, PRTN3), HSC (CD34, PROM1), Late pro-B cells (CD19, CD79B, DNTT, RAG1), Monocytes/Macrophages (CD68), MSC (LEPR, CXCL12, ANGPT1), T cells/NK cells (CD3D, CD8A, NKG7), Plasma cells (CD79B, JCHAIN, MZB1), Pro-B cells (CD19, CD79B, EZH2), Pro-Erythroblast (HBB, TFRC, MKI67).

ATAC-Seq and bioinformatics analysis

ATAC-Seq libraries were made form sorted BM $CD7^+$ monocytes as indicated using GenSeq ATAC kit (GenSeq). The libraries were quantified using Qubit fluorometric assay (ThermoFisher) and then sequenced in a NovaSeq platform (Illumina) by CloudSeq Biotech (Shanghai, China). After Illumina NovaSeq6000 sequencer sequencing, image analysis, base identification, and quality control, raw reads are generated. First, use Q30 for quality control. Then, use the cutadapt software (v1.9.1) to remove the connectors and remove low-quality reads to obtain high-quality clean reads. Use bowtie2 software (v2.2.4) to compare clean reads to the reference genome. Use MACS software to identify open chromatin regions (enriched peaks) (Peak Calling), and use bedtools software (v2.24.0) to annotate enriched peaks, link peaks, and genes information. Use IGV software (v2.64) to visualize the enrichment peaks.

Flow cytometry

Mouse BM immune cells and BMMs were collected and preincubated with APC-Cy7 Zombie Dyes for 10 min at room temperature. Cells were subsequently stained with CD7 antibody (Proteintech) for 60 min at 4 °C, and then incubated with Alexa fluor 488-anti mouse IgG (Invitrogen), BV510-anti mouse/human CD11b, PE-anti mouse Ly6G, PE-Cy7-anti mouse Ly6C for 30 min at 4 °C. The $CD11b^+Ly6G^-$ $Ly6C^+CD7^-$ cells were sorted as mouse $CD7^-$ monocytes. The $CD11b^+Ly6G^-Ly6C^+CD7^+$ cells were sorted as mouse $CD7^+$ monocytes. The peripheral blood cells from post-dieting donors were stained with CD7 antibody (Proteintech) for 60 min at 4 °C and then stained with Alexa fluor 488-anti mouse IgG (Invitrogen), BV510-anti mouse/human CD11b, and Percp-anti human CD14 for 30 min at 4 °C. The $CD11b^+CD14^+CD7^-$ cells were sorted as human $CD7^-$ monocytes. The $CD11b^+CD14^+CD7^+$ cells were sorted as human $CD7^+$ monocytes. Stained cells were immediately sorted by flow cytometry Aria (BD Biosciences), routinely to more than 95% purity. Cell surface markers were stained by incubating cells with antibody solutions for 30 minutes at 4°C in dark. Anti-GPR183 antibody (Alomone labs) and biotin Flt3 antibody, coupled with corresponding fluorescent secondary antibody, were used to stain the cell surface expression of GPR183 and Flt3 when indicated.

The $CD3^-CD19^+GL7^+$ cells were defined as active B cells. The $CD3^+CD4^+CD69^+$ cells were defined as active $CD4^+$T cells, $CD3^+CD8^+CD69^+$ cells were defined as active $CD8^+$T cells, and $CD3^-CD69^+NK1.1^+$ cells were active NK cells. While $CD4^+Foxp3^+CD44^+$ cells were active Treg cells, $CD11b^+Ly6C^+CD86^+$ cells were regarded as active monocytes and macrophages.

For cell-cycle analysis, surface labeled BM immune cells were fixed, permeabilized, and stained with Ki67 (Proteintech) and CD7 antibody (Proteintech) for 60 min at 4 °C, then incubated with indicated antibodies for 30min 4 °C. $Ki67^-DAPI^-$ cells were in G0 phase, $Ki67^+DAPI^-$ cells were in G1 phase, and $Ki67^+DAPI^+$ cells were in S-G2-M phase. Data were analyzed by FlowJo V10 (BD

Biosciences). Unless otherwise stated, all antibodies are commercially available from BioLegend. All antibodies were diluted according to the manual from the manufacturer's website. Data were analyzed by FlowJo V10 (BD Biosciences).

Adoptive transfer of human CD7$^+$ monocytes

NOD.Cg-Prkdc^{scid}Il2rg^{em1Smoc} (NSG) mice were housed at 30°C for 4-week HFD feeding to induce body weight gain. To investigate the metabolic effects of human CD7$^+$ immune cells, isolated human CD7$^+$ monocytes and CD7$^-$ monocytes were transferred into these pre-obese mice intravenously (2 x 10^5 cell /300 μl / mice) and mice were kept on HFD for another 6 weeks before being euthanized.

Bone-marrow chimeric mice construction

Wile-type C57BL/6 CD45.2 male mice were lethally irradiated (950 cGy) and adoptively transferred with 1 × 10^7 BM immune cells from CD45.1 donor mice intravenously within 24 h after irradiation exposure. The reconstitution effect was detected five weeks after BM cell transplantation.

In vivo tracing of CD7$^+$ monocytes distribution

To investigate the distribution of CD7$^+$ monocytes, BM cells from Cyc mice were stained as described and collected by flow cytometry sorting. The sorted cells were labeled with the lipophilic dye DiR iodide (Invitrogen) according to the manufacturer's instructions for ex vivo optical imaging. The labeled cells were suspended in PBS (5 × 10^5 cells in 300 μl PBS) and injected into the mice through tail-vein. Three days later, all mice were euthanized to collect the brown adipose tissue, subcutaneous adipose tissue, epididymal adipose tissue and bone. Fluorescent signals in these tissues were detected immediately and quantified with a fluorescence tomography imaging system (FMT-4000; PerkinElmer, USA). Similarly, the sorted CD7$^+$ monocytes were labeled with lipophilic dye PKH26 (Sigma) according to the instructions and injected into mice intravenously. One week after injection, the adipose tissues were collected and fixed in 4% paraformaldehyde for 24 h and then embedded in an optimum cutting temperature compound at −20 °C. Ten-micrometer-thick slices were obtained to observe the fluorescence signals of PKH26 under a fluorescence microscope.

siRNA-mediated gene knockdown

The sorted mouse CD7$^+$ monocytes were cultured in culture in RPMI 1640 (Gibco) supplemented with 10% FBS, 100 U/ml penicillin, and 100 μg/ml streptomycin. The sorted cells were transfected with *Gpr183*-targeted siRNA (si-*Gpr183*) or matched control (si-Scramble). 24h after transfection, the sorted cells were collected, labeled with lipophilic dye PKH26 (Sigma) according to the instructions, and transferred into recipient mice as indicated through tail-vein injection. One week after injection, the adipose tissues were collected and fixed in 4% paraformaldehyde for 24 h and then embedded in optimum cutting temperature compound at −20 °C. Ten-micrometer-thick slices were obtained to observe the fluorescence signals of PKH26 under a fluorescence microscope. Alternatively, *Tmem120a*-targeted siRNA (si-*Tmem120a*) or matched control (si-Scramble) were transfected into beige adipocytes before being treated with rFGL2.

Cold exposure experiment

Mice were single-housed in cages without bedding at 6 °C with ad libitum feeding. During the experiment, core body temperature was measured hourly. At the end of the experiment, mice were euthanized and fat tissues were isolated to determine thermogenic gene and protein expression.

Comprehensive lab animal monitoring system

Indirect calorimetry experiments were conducted with a Comprehensive Lab Animal Monitoring System (CLAMS, Columbus Instruments). Mice in the CLAMS were maintained at either room temperature (25°C) or cold (4°C) conditions for a total of 3 days and fed ad libitum. Results of oxygen consumption, energy expenditure, activity, and RER were collected and analyzed.

Glucose tolerance test (GTT) and insulin tolerance test (ITT)

Male mice at 8 weeks of age or after BM reconstitution were fed a ND or a HFD (60% of calories from fat, Research Diets) for 8–12 weeks as indicated. For GTT, mice were fasted overnight and challenged with an intraperitoneal injection of glucose (2 g/kg). For ITT, mice were fasted for 6 h, followed by an intraperitoneal injection of insulin (0.75 U/kg). Blood glucose levels were monitored using the ACCU-CHEK active glucometer (Roche).

Bone marrow monocytes and macrophages isolation

Mouse BM-derived monocytes and macrophages (BMMs) were isolated as previously described.[42] In brief, BM cells were flushed and cultured in α-MEM (Gibco) with 10% FBS, 100 U/ml penicillin, and 100 μg/ml streptomycin overnight. The floating cells were collected and cultured in the culture medium added with 50 ng/ml M-CSF (Proteintech) to obtain BMMs.

Protein treatment

Recombinant mouse FLT3 ligand (FLT3L) and recombinant mouse FGL2 (rFGL2) were purchased from Sinobiological and MedChem Express, respectively. Cyc-10w mice were treated with 2 μg FLT3L protein per mouse three times a week for two weeks or ten weeks

as indicated. BMMs were treated with FLT3L protein at the indicated concentration and time. For rFGL2 protein, mice were treated with a daily tail-vein injection of 0.4 μg rFGL2 protein per mouse in 200μl PBS for 7 days and subjected to cold exposure. Otherwise, mice were treated with 50 μg/kg rFGL2 protein every other day for 6 weeks. Beige adipocytes were treated with rFGL2 protein at the indicated concentration and time.

Seahorse Cell Mito Stress Test

The Seahorse Bioscience XFe96 FLUX Analyzer (Agilent) was used to measure the OCR or ECAR of $CD7^+$ and $CD7^-$ monocytes. In brief, $CD7^+$ and $CD7^-$ monocytes were isolated form Cyc mice by flowcytometry sorting, and seeded at a density of 1.5×10^5 cells/well into poly-L-lysine coated 96-well plates, cultured in RPMI 1640 (Gibco) supplemented with 10% FBS, 100 U/ml penicillin, and 100 μg/ml streptomycin and allowed for adherent to the bottom overnight. Cells were incubated with RPMI 1640 containing 25mM D-glucose, 2mM sodium pyruvate and 2mM L-glutamine for 1h at 37°C without CO2 prior to measurement. The mitochondrial stress test utilizes sequential injections of 1μM oligomycin A (Glpbio), 2μM carbonyl cyanide 4-(trifuoromethoxy) phenylhydrazone (FCCP, Sigma), and 1μM rotenone (Sigma)/antimycin A (Glpbio). The parameters of OCR and ECAR were automatically calculated by the WAVE desktop software (Agilent). All parameters were normalized to total protein amount in each wells using BCA protein assay (Elabscience).

Isolation of mouse and human T cells

Moues T cells were also isolated from the spleen by magnetic beads separation system using a mouse $CD4^+$ T cell isolation kit (Miltenyi Biotec) as previously described.[18] The peripheral blood cells from post-dieting donors were stained with APC-anti human CD4 (Biolegend) and APC/Cy7-anti human CD3 (Biolegend) for 30 min at 4 °C, and the $CD3^+CD4^+$ cells were sorted as human T cells.

Co-culture experiment

To investigate the effects of $CD7^+$ monocytes on proliferation and inflammatory cytokine production of $CD7^-$ monocytes and T cells, $CD7^+$ monocytes were co-culture with $CD7^-$ monocytes or $CD4^+$T cells in both contact and non-contact way. Briefly, mouse and human $CD7^+$ and $CD7^-$ monocytes were isolated from Cyc mice and post-dieting donors by flow cytometry sorting, respectively. For contact co-culture, $CD7^+$ monocytes and $CD7^-$ monocytes were directly seeded into 96-well plates at the ratio of 1:1; $CD7^+$ monocytes and $CD4^+$T cells were directly seeded into 96-well plates at the ratio of 1:3. For non-contact co-culture, $CD7^+$ monocytes were seeded in the upper chamber of 24-well Transwell plates (3 μm pore size, Corning), $CD7^-$ monocytes or $CD4^+$T cells were seeded in the bottom chamber at the same ratio of contact co-culture. After 48h co-culture, $CD7^-$ monocyte and $CD4^+$T cells were collected for cell cycle analysis, and the cell supernatant were used for measurement of IFN-γ and TNF-α levels.

Transwell migration assay

$CD7^-$ and $CD7^+$ monocytes were isolated by flow cytometry from Cyc mice, and 5×10^5 $CD7^-$ and $CD7^+$ monocytes were placed in 24-well Transwell plates (8μm pore size, Corning). The bottom chambers were filled with various concentrations of 7α,25-Dihydroxycholesterol (MedChem Express) suspended in serum-free medium. Plates were cultured for 3 h at 37 °C, at which point migrated monocytes were collected from the lower chamber and cells were counted in a blood cell counting chamber under light microscopy.

Pull down assay and mass spectrometry analysis

In vitro pull-down assay and mass spectrometry analysis were applied to screen candidate membrane receptors for FGL2 protein in adipocytes. Briefly, HEK293T cells were transfected with His-FGL2 plasmid. After 24h, cell supernatant was collected every 24h and concentrated by using 50kDa centrifugal filter (Millipore) to produce His-labelled FGL2 protein. C3H10T1/2 preadipocytes (Procell) were cultured and induced to adipogenic differentiation as previously described.[41] Membrane protein of differentiated C3H10T1/2 beige adipocytes were isolated using membrane protein extraction kit (Beyotime Biotechnology) according to the manufacturer's manual. For pulldown assay, isolated adipocyte membrane proteins were incubated with His-labelled protein and His antibody (Cell Signaling Technology) at 4°C overnight, followed by adsorption to protein A/G magnetic beads (MedChem Express) at room temperature for 1h. The magnetic beads were washed, magnetically separated and eluted. The eluted protein sample was subjected to mass spectrometry analysis using Q Exactive mass spectrometer (Thermo Fisher Scientific) under the help of APTBIO (Shanghai, China).

Molecular docking analysis

The X-ray crystal structures of TMEM120A (PDB: 7N0K) were retrieved from the Protein Data Bank. The predicted structures of FGL2 were generated by Alphafold (AlphafoldDB: P12804). Docking Web Server (GRAMM) was used for protein-protein docking.[43,44] The protein and resulting protein-protein complex was manually optimized by removing water and adding polar hydrogen by the AutoDockTools-1.5.7.[45] The figure of predicted protein-protein interactions was generated by PyMOL.

ELISA

The concentration of FGL2 in serum or cell supernatant was measured by using FGL2 ELISA kit (Abcam). The serum concentration of AGRP, NPY, Ghrelin and Leptin were determined by using ELISA kit from Jingmei Biotechnology and 4A Biotech. The level of serum IFN-γ and TNF-α or cell supernatant were measured by using ELISA kit from 4A Biotech. All measurements were performed accordingly to manufacturer's instructions.

Co-IP and Western blot analysis

Co-immunoprecipitation was performed as described previously.[46] Briefly, HEK293T cells were co-transfected with HA-TMEM120A plasmid together with FLAG-FGL2 plasmid or truncated FLAG-FGL2 plasmid for 48 h. Total cell lysates were collected and immunoprecipitated by incubation with antibodies against HA (Cell Signaling Technology) and FLAG (Cell Signaling Technology), respectively followed by adsorption to protein A/G magnetic beads (MedChem Express). Western blot analysis was performed as previously reported.[47] Briefly, immunoprecipitates or lysates of cells and tissues were separated by SDS-PAGE and blotted on PVDF membranes. The membranes were blocked in 5% non-fat milk, then incubated in the primary antibody at 4°C overnight, followed by incubation with HRP-conjugated secondary antibodies at 37°C for 1 h. The primary antibodies used are UCP1 (Abcam), PGC-1α (Santa Cruz Biotechnology), FGL2 (Proteintech), HA (Abmart), FLAG(Origene), TMEM120A(Proteintech), cAMP (Abcam), p-PKA (Cell Signaling Technology), CREB1 (Proteintech), p-CREB (Cell Signaling Technology), α-Tubulin (Proteintech), GAPDH (OriGene) and β-Actin (Proteintech).

Histochemistry, Immunohistochemistry, and Immunofluorescence

H&E staining, immunohistochemical staining and immunofluorescence staining were performed as described.[41] Briefly, isolated mouse and human adipose tissues were fixed, dehydrated, embedded in paraffin, and sectioned. The sections were dewaxed, hydrated, heat-retrieved, blocked and subjected to incubation of primary and secondary antibodies. The primary antibodies used in immunohistochemistry staining are anti-UCP1antibody (Abcam). The primary antibodies used in immunofluorescence are anti-human CD68 antibody (Servicebio) and anti-CD7 antibody (Proteintech).

qPCR Analysis

Total RNAs were extracted from tissue or cultured cells using AG RNAex Pro Reagent (Accurate Biotechnology (Hunan)). The cDNA synthesis and qPCR assay were performed as previously described.[48] The relative mRNA levels were calculated by the $2^{-\Delta\Delta Ct}$ method using β-Actin as an internal control. The primer pairs used for qPCR were listed in Table S2.

QUANTIFICATION AND STATISTICAL ANALYSIS

All data are presented as mean ± SEM from at least 4 biological replicates and are representative of 3 technical replicates. Two-tailed Student's t-test was used for comparisons between two groups, and one- or two-way ANOVA were used for comparisons among multiple groups with Bonferroni's multiple-comparisons test. Pearson's Correlation analysis was used for the correlation coefficient. The Analysis of Covariance (ANCOVA) test was performed to analyze differences in oxygen consumption and energy expenditure between the groups while statistically controlling for the effects of covariate body weight.[49] All animal experiments were repeated at least three times, and representative experiments are shown. Significance in all Figures is denoted as follows: *$p < 0.05$, **$p < 0.01$, ***$p < 0.001$.